Wear 490–491 (2022) 204184

Contents lists available at ScienceDirect

Wear

journal homepage: www.elsevier.com/locate/wear

Ambient dry sliding friction and wear behaviour of laser surface textured (LST) Ti_3SiC_2 MAX phase composite against hardened steel and alumina

ARTICLE INFO

Keywords
MAX phase
Ti_3SiC_2
Laser surface texturing
dry sliding wear

ABSTRACT

This paper investigates the feasibility of improving the tribological properties of Ti_3SiC_2 MAX phase composite by employing laser surface texturing (LST). Two different surface textures (line and square) were produced on the bulk sample using a continuous laser. The friction and wear performance of the line and square textured surface was investigated against an untextured surface following reciprocating dry-sliding contact against hardened steel and alumina counterface at ambient conditions. Sliding-induced chemical and topographical changes were studied by 3D optical profilometry, Raman spectroscopy, and scanning electron microscopy. Test results show that both the line and square textured MAX phase composite surface exhibit excellent wear performance as well as a reduction in friction. The improved performance is linked to the combined effect of surface texture, topography, surface hardening and tribofilm evolution. The type of counterface material played a vital role in the nature of tribo-oxidation product formed as well as the extent of wear of the MAX phase material.

1. Introduction

Titanium silicon carbide (Ti_3SiC_2) is a representative metalloceramic because of its unique and unusual dual metallic and ceramic properties and belongs to the MAX phase family with chemical formula generated from $M_{n+1}AX_n$ chemistry – where n = 1, 2, 3 or higher, M is an early transition metal, A is an A-group element (mostly groups 13 and 14), and X is C or N [1,2]. The crystal structure of Ti_3SiC_2 consist of a two-dimensional closed packed layers of Si periodically intercalated into the (111) twin boundary of $TiC_{0.67}$ (Ti_3C_2) [3]. As such, the formation of Ti_3SiC_2 during synthesis involves the transformation of cubic $TiC_{0.67}$ following silicon intercalation to hexagonal Ti_3SiC_2 [3]. Along with several members of the MAX phase family, titanium silicon carbide (Ti_3SiC_2) has been proposed for a range of structural applications owing to its low hardness, light weight, easy machinability, good electrical and thermal conductivities, high modulus and thermal shock resistance [4–6]. These layered solids lack the five independent slip systems needed for ductility [7]. Nonetheless, they possess abundant basal plane dislocation (BPD) [8] – which are mobile and tend to multiply at room temperature – that enables them to deform by kink band (KB) [9,10] and ripplocation formation [11,12]. In contrast to other advanced ceramics, they exhibit better damage tolerance which is readily observed following Vickers indentation. Instead of crack formation and propagation, energy absorbing microscale mechanisms such as delamination, kinking of individual grains, and grain pullouts activates in the vicinity of the indent [13–17]. The reported fracture toughness of polycrystalline MAX phases ranges from 5 to 8 MPa $m^{1/2}$ [8], whilst higher values have been reported for Ti_3SiC_2 (11.50 MPa $m^{1/2}$) [18] and Nb_4AlC_3 [19], respectively.

Ti_3SiC_2 has also been considered as a single component solid lubricant for different tribological applications due to its intrinsic lubricity and layered structure similar to well-known solid lubricants such as graphite and MoS_2 [20]. Although Ti_3SiC_2 possesses low friction properties [21–24], and in some cases ultra-low friction has been reported [25]. However, Ti_3SiC_2 is in fact susceptible to grain boundary fracture and grain pull-out due to its low grain boundary strength, leading to a three-body wear in reported wear studies [26–28]. Friction and wear behaviour of Ti_3SiC_2 against steel was investigated by Tamer et al. [26]. They observed an initial friction coefficient transition from 0.15 to 0.45, followed by a steady rise in friction coefficient to steady values to about 0.83. It was concluded that, the transition from low to high friction coefficient is due to accumulation of debris trapped between the disc and the pin – and this resulted in third-body abrasion. Shufang et al. [29] studied the elevated temperature tribological behaviour of Ti_3SiC_2 sliding against Ni-based alloy. They attribute the poor tribological response to the fracture and pullout of Ti_3SiC_2 grains. The relatively low hardness of Ti_3SiC_2 under high hardness counterpart during ambient dry sliding contact was reported to induce high stress concentration and rough worn surface which led to severe wear [30].

One strategy to solve these problems is to encourage the formation of TiC and/or SiC intermetallic phase(s) in the matrix of Ti_3SiC_2 during its synthesis. Guo et al. [31] improved the surface hardness and wear resistance of Ti_3SiC_2 by forming TiC_x. Previous work has shown that these intermetallic particles segregate preferentially along the grain boundary, thus improving the grain boundary strength which in turns inhibits the ease of grain pull-out [22,32,33]. Another solution to the poor grain boundary strength in MAX phases, which deteriorates their load bearing capacity, is the introduction of micro-irregularities via laser surface texturing; as this may help enhance their load bearing capability during sliding contact [34,35]. Surface texturing involves controlled modification of topography to produce functional surfaces [36–38]. It is common knowledge that energy dissipating sliding contact events during dry-sliding, such as ploughing by asperities and/or wear debris, adhesion, elastic and plastic deformation, and fracture, are highly

https://doi.org/10.1016/j.wear.2021.204184
Received 6 September 2021; Received in revised form 9 November 2021; Accepted 11 November 2021
Available online 26 November 2021

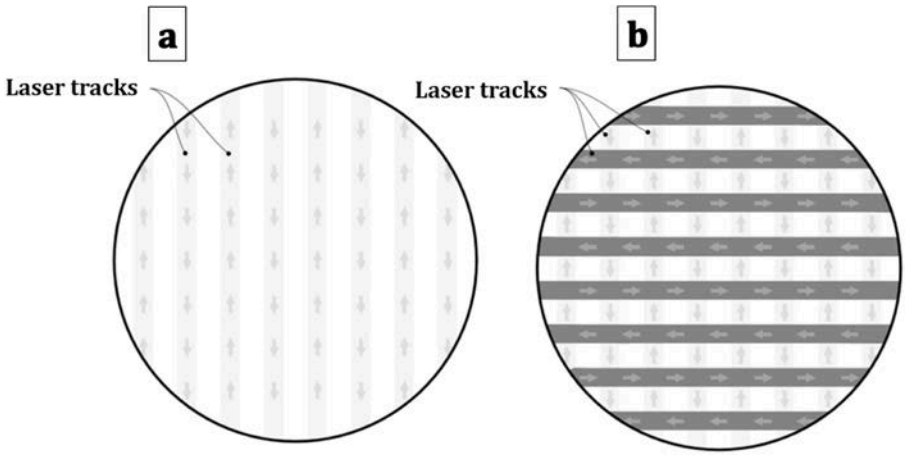

Fig. 1. (a) Laser surface texturing for line scans (arrows indicates the direction of the laser movement) and (b) second pass over the first pass to create square patterns.

Table 1
Starting surface roughness (Ra) of bulk samples and counterbodies.

Bulk disc sample			Counterbody	
Untextured	Line Textured	Square Textured	Al_2O_3	Steel
0.03 μm	1.76 μm	6.11 μm	0.06 μm	0.07 μm

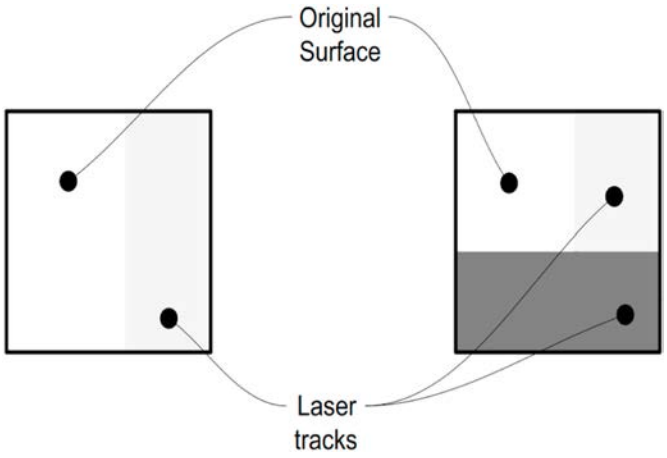

Fig. 2. Schematic of line (left) and square (right) texture patterns showing the original surface and laser track paths from which the section area was estimated.

dependent on surface topography [39]. As such, surface texturing has the potential to improve friction and wear [39,40].

Laser surface texturing (LST) as a means for enhancing tribological performance of mechanical components has been extensively studied [40–46]. An additional benefit of employing laser surface texturing, particularly a continuous wave (CW) laser as compared to other surface texturing techniques, is that laser processing induces local non-equilibrium microstructural changes on the textured surface, which can enhance performance [47]. Some of the tribological effects of surface texturing are summarised as follow: entrapments of wear particles – generated during rubbing – in the recesses to minimize friction [48], ploughing and damage to the surface [34], decrease in contact area by producing an additional lift effect [49], improvement in load-carrying capacity [50], reduction of scuffing and adhesion [51], activation of tribofilms via stress-induced tribochemical reactions due to increased contact pressure at texture edges [52,53], improved heat transfer from the sliding surface – this help to decrease localized temperature build-up – to bring about wear reduction [40], as well as the recesses acting as reservoirs for lubricant retention which help release lubricious material to sliding contact gradually during sliding [41].

However, despite the promise of this surface engineering technology, there is an obvious limitation under high load and low sliding speed [51,54]. This is because under such sliding conditions, surface textures may be worn quickly and potentially lead to the generation of abrasive wear debris that accelerates wear. Furthermore, surface textures under dry sliding conditions may induce undesired effects [54], such as increased stress concentrations at the contacting points owing to the reduced contact area, which will inevitably lead to increased wear [55,56]. A potential strategy as proposed Rosenkranz et al. [40] to mitigate these short-comings involve combining surface texturing with a layered material. This concept lies on exploiting the synergetic contribution of both texturing and layered material, i.e. the surface texture entraps wear particles and decrease contact area whilst the layered material facilitates sliding owing to their weekly bonded planes of atoms.

The literature on the laser surface texturing of MAX phases is sparse. The only literatures reported to date are on the wetting behaviour of laser textured Ti_3SiC_2 [35], and more recently, a study on the fretting wear of laser textured Ti_3SiC_2/GNP composite [57]. In our previous studies on the tribology of Ti_3SiC_2 [28,58] as well as those from other investigators [20,23], it has been established that the MAX phase Ti_3SiC_2 is indeed intrinsically lubricious. However, its susceptibility to wear debris-induced abrasive wear, ease of grain pullout during sliding contact, and poor load-bearing capacity due to its low hardness deteriorates its wear properties. The motivation of this work is to investigate how surface texturing most essentially can mitigate some of these short-comings that deteriorate the wear behaviour of Ti_3SiC_2. An important concept to be exploited in this work is to see if indeed trapping wear debris within recesses created by laser texturing will improve the wear properties. We also know from previous studies that at high temperature, Ti_3SiC_2 will decompose into binary carbide TiC_x due to silicon de-intercalation [59]. As such, surface texturing especially in this study which incorporates a continuous laser will induce high surface heat enough to cause a phase transformation from hexagonal Ti_3SiC_2 to cubic TiC_x at the surface. The formation of TiC at the laser textured surface will help improve the load bearing capacity of the underlying Ti_3SiC_2 below the textured surface. Also, by encouraging the in-situ formation of TiC particles in the Ti_3SiC_2 matrix during synthesis may provide some pinning effect on the Ti_3SiC_2 grains – and this will likely inhibit the ease of grain pullout [33].

Motivated by the aforementioned possible surface texture-induced

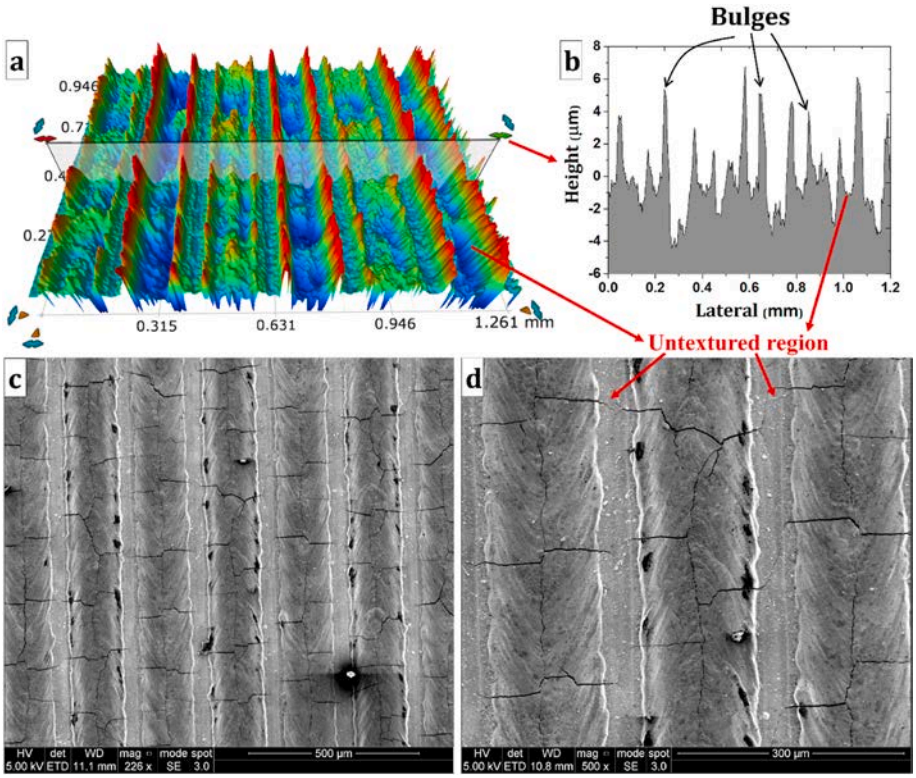

Fig. 3. (a) 3D surface topography of the line texture, (b) cross-section profile scan showing the depth of the texture and height of the bulges, and (c–d) low and high magnification secondary electron SEM images showing the line texture pattern alongside with evidence of laser texture-induced microcracking.

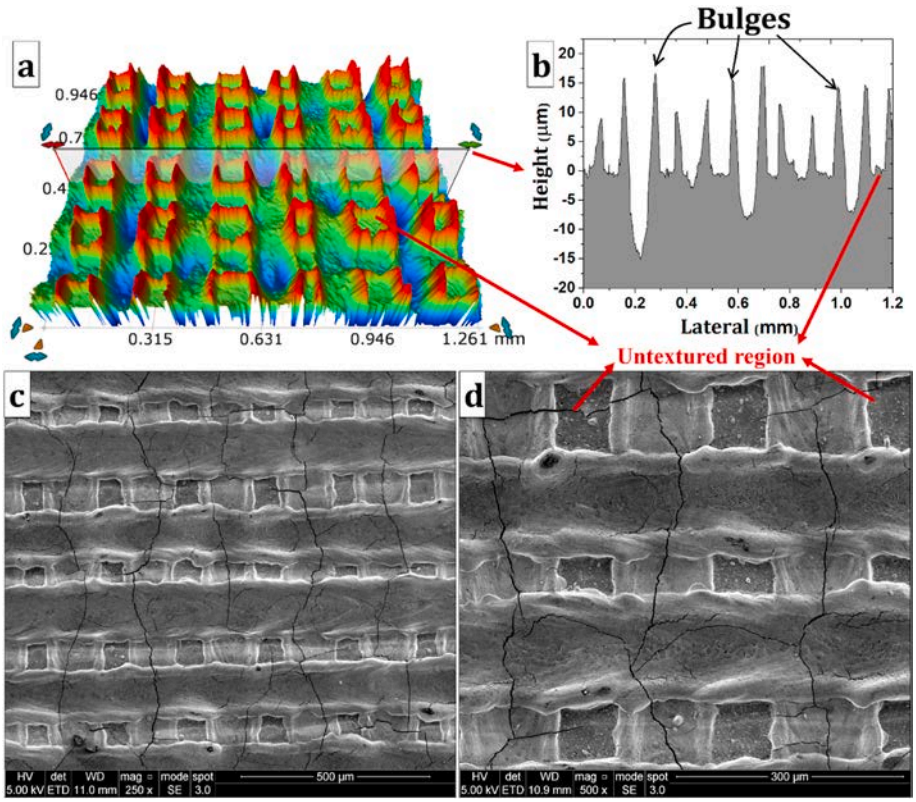

Fig. 4. (a) 3D surface topography of the square texture, (b) cross-section profile scan showing the depth of the texture and height of the bulges, and (c–d) low and high magnification secondary electron SEM images showing the square texture pattern alongside with evidence of laser texture-induced microcracking.

Table 2
Estimated texture parameters for the line and square patterned specimens.

Texture parameters	Line pattern	Square pattern
Texture density (%)	73	88
Texture depth (H/μm)	12	30

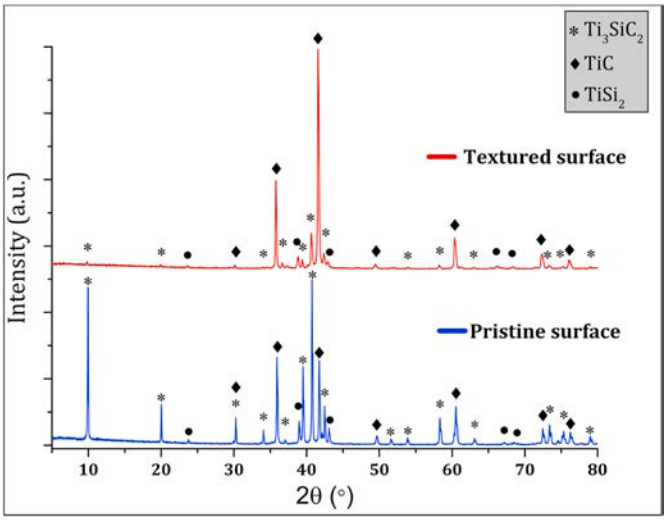

Fig. 5. X-ray diffraction (XRD) patterns corresponding to the pristine surface (untextured) and laser textured surface.

properties and features, this study exploits the use of laser surface texturing to mitigate some of the factors responsible for the increase in wear rate of Ti_3SiC_2 MAX phase – and most especially third-body abrasive wear debris formation. It is noteworthy that this study will not cover the role of different texture geometry as well as depth and density of pattern, even though they play an important role on tribological performance [44]. Instead, the focus of this study is to investigate the influence of surface texture on the evolution of topography, microstructure and chemistry at the surface. These will help to answer the following questions such as: (1) Does wear debris entrapment in recesses created by surface texture improves friction and wear; (2) Does surface texture-induced phase transformation brings about hardening; (3) What is the role of surface texture on tribofilm formation; (4) What is the influence of increase in surface roughness (Ra) following surface texture on friction evolution and (5) What is the implication of surface texture on wear of counterparts.

2. Experimental procedure

2.1. Materials and process methods

Bulk non-monolithic polycrystalline MAX phase samples were fabricated by using a starting prealloyed MAX phase powder (2,5 μm, Maxthal 312 (nominally Ti_3SiC_2) – Kanthal AB Sweden). The starting powder contained about ~92 wt% Ti_3SiC_2 and 8 wt% TiC as ancillary phase. The powder was synthesized by spark plasma sintering (SPS) using sintering parameters: 1350 °C sintering temperature; heating rate 100 °C/min; pressure 16 kN and 10 min dwell time. The sintering parameters were chosen to correspond to the onset of the decomposition of Ti_3SiC_2 into TiC_x as the scope of this work is to encourage the formation of second phase TiC particle in the Ti_3SiC_2 matrix. Further details on the

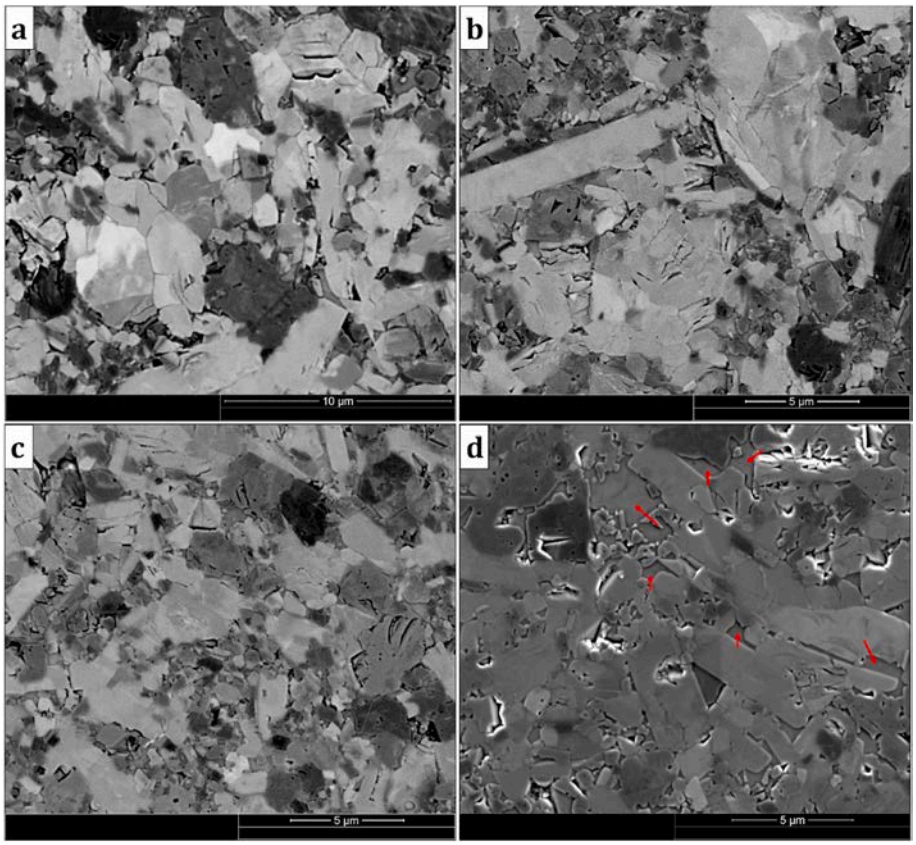

Fig. 6. Scanning electron micrograph showing the typical morphology of the as-synthesized bulk sample. (a), (b) and (c) are backscattered electron (BSE) micrographs showing the Ti_3SiC_2 phase (bright contrast) and TiC phase (dark contrast), and (d) is a secondary electron (SE) micrograph showing the $TiSi_2$ liquid phase pockets (red arrows). (For interpretation of the references to colour in this figure legend, the reader is referred to the Web version of this article.)

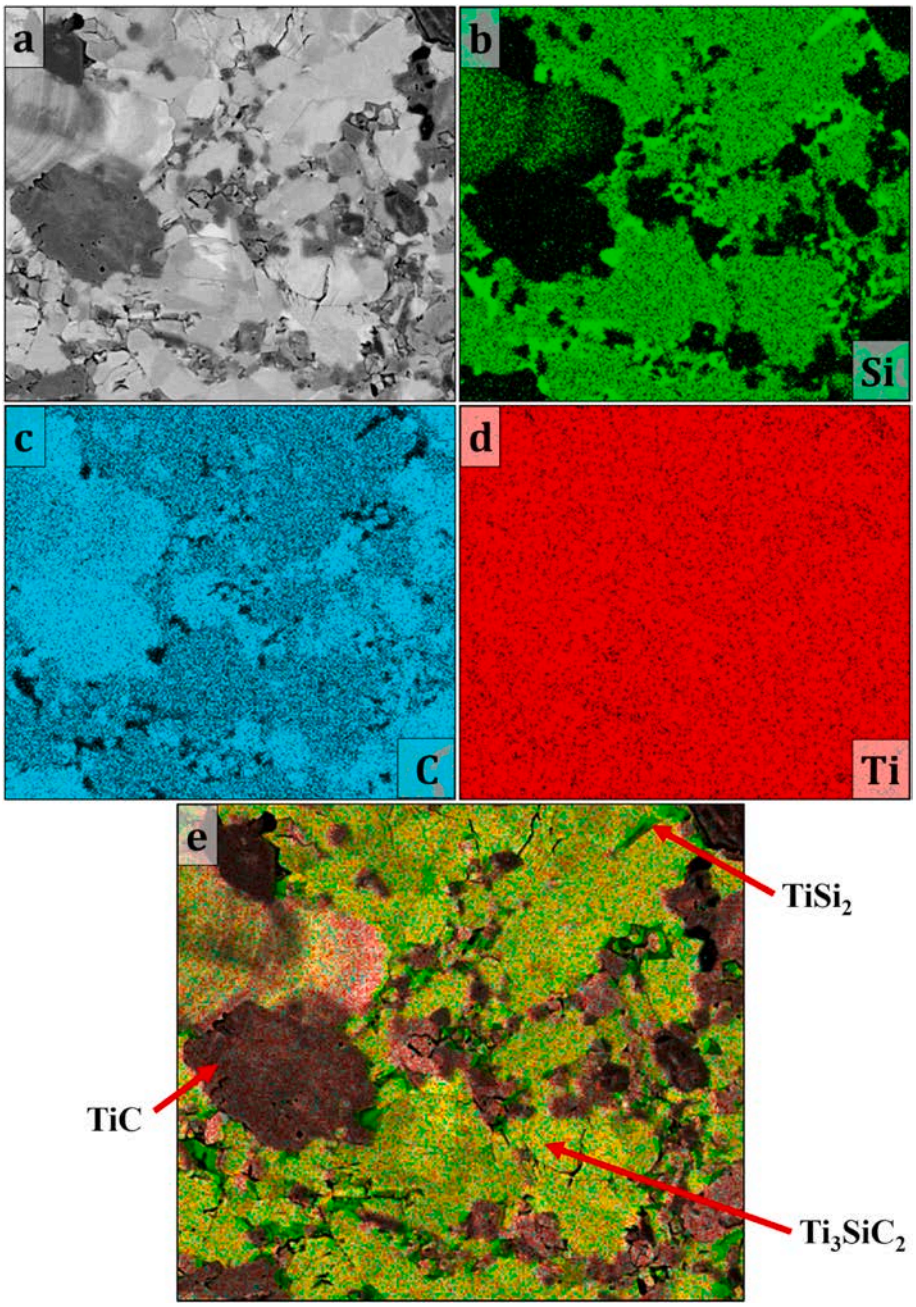

Fig. 7. EDS elemental map distribution collected from the electron image showing the distribution of Si, C, and Ti alongside the identification of the Ti_3SiC_2 phase, TiC phase and $TiSi_2$ phase, respectively.

powder consolidation and SPS synthesis can be found elsewhere [59]. Following SPS, the sintered compacts were first ground to remove any surface carbide layer contamination which can result from the SPS graphite-rich sintering tools, and then polished to a mirror finish. The density of the sintered compact was determined by Archimedes method and the relative density obtained by comparison to the theoretical densities of the respective phases in the bulk sample.

Phase composition of the sintered polished sample was analysed using X-ray diffractometry (Bruker D2 Phaser) with CuKα radiation at a scanning speed of 0.02°/s and a 2Θ range of 5–80°. Microstructure and morphology of the pristine, textured and worn surfaces were examined by scanning electron microscopy (SEM: Inspect F50, FEI, Netherlands) to understand the underlying mechanism(s). The microhardness was measured using a Durascan microhardness tester (G5 emcoTEST, Austria) at 4.9 N with a dwell time of 15 s. To understand the chemical interactions of tribopairs, Raman spectra point analyses of the evolved chemistry at the sliding surface was investigated ex-situ by employing a Si-calibrated Raman spectrometer (inVia Renishaw, UK) equipped with an Ar laser ($\lambda = 514.5$ nm, laser output power 20 mW). The roughness of the bulk samples and the balls before the wear test were obtained using an optical profiler. 3D topography and surface profile of the pristine, textured and worn surfaces were obtained using a noncontact 3D optical profiler (Contour Elite X, Bruker) equipped with vision 64® analysis software. Tribological investigations were performed using a friction and wear testing machine (Tribolab, Bruker, USA) with a ball-on-disc contact configuration adopted under unlubricated ambient reciprocating sliding conditions. The MAX phase samples (in total three samples) were prepared as a disc (Ø = 20 mm) with the surface polished down to a 0.5 μm diamond finish before laser texturing and wear testing. The counterface was a 4 mm diameter spherical Al_2O_3 ball and a

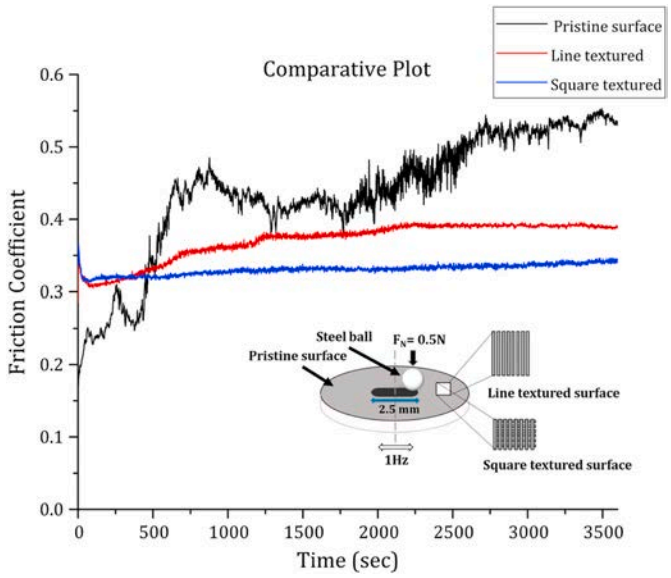

Fig. 8. Evolution of friction coefficient of the pristine/untextured surface (in black), line textured (in red) and square textured (in blue) samples after sliding against hardened steel ball. (For interpretation of the references to colour in this figure legend, the reader is referred to the Web version of this article.)

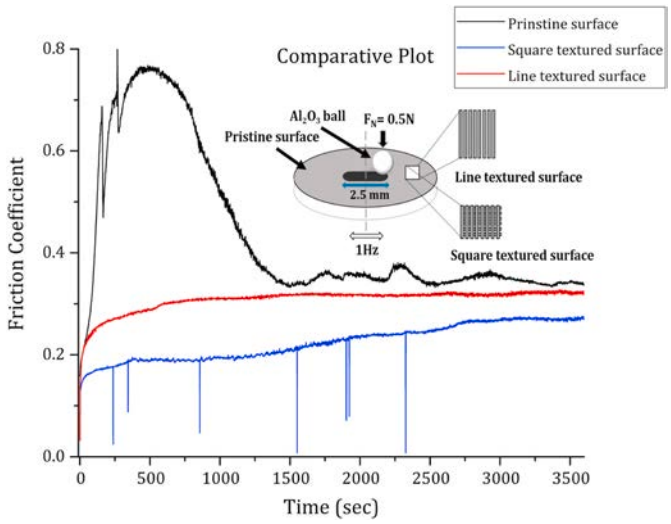

Fig. 9. Evolution of friction coefficient of the pristine/untextured (in black), line textured (in red) and square textured (in blue) samples after sliding against alumina (Al_2O_3) ball. (For interpretation of the references to colour in this figure legend, the reader is referred to the Web version of this article.)

hardened steel ball (AISI 52100 – component element of the steel (carbon (0.98–1.1%), chromium (1.3–1.6%), manganese (0.25–0.45%), phosphorus (0.025%), silicon (0.3%) and sulphur (0.025%)) of the same dimensions. Prior to friction and wear testing, the ball and disc specimens were cleaned with isopropanol. The sliding friction and wear test conditions were: a normal force of 0.5 N (Maximum contact pressure $P_{max} = 180$ MPa), stroke length of 2.5 mm, frequency 1 Hz (0.005 ms^{-1}), sliding time of 60 min, total sliding distance of 18 m, temperature 25 ± 2 °C, and 37% RH. For the textured surfaces, wear testing was conducted perpendicular to the textured patterns. Previous work by numerous investigators has shown that sliding orientation plays a vital role in tribological performance due to differences in contact area [48,60,61]. Low friction coefficients have been reported for the perpendicular sliding orientation as compared to parallel orientation [51,62–64]. Additionally, our initial judgement was that sliding parallel to the texture especially for the line textured pattern will lead to continuous contact point as well as the wear debris generated being continuously moved in the sliding direction rather being left behind in the cavities.

The sliding wear test was repeated at least three times on each sample surface (that is, line texture, square textured and untextured) to ensure repeatability. The worn volume was extracted directly from the software which takes into account the full wear scar rather than several profilometric scans across the wear track. The specific wear rate of the ball and disc specimens was calculated using the following standard equation:

$$W = \frac{V}{N.l}$$

where V is the wear volume, N is the normal load applied, and l is the total sliding distance.

The test conditions have been chosen carefully to fulfil the following rationale:

1) As part of the aim of this work is to investigate the suitability of MAX phase as solid lubricants (that is, thin films) in aerofoil bearings which rely on self-lubricants to reduce friction and minimize wear especially during start-up and shut-downs sliding which occurs at low loads and sliding speed [20,65]. Typical load ranges from 0.2 to 1 N over a wide range of temperatures [65]. Such tribosystem (i.e., air foil bearings (AFBs)) often incorporates a metal such as Ni-based super alloy and/or stainless coated with low friction material. In this work alumina was chosen as counterface material because it is inert and will not be expected to react with the bulk sample – thus making it possible to investigate the intrinsic lubricity of the MAX phase material. Hardened steel on the other hand was chosen over stainless steel due to its hardness and better load-bearing capacity as compared to stainless steel. It is also expected that iron-oxide tribofilm will be adherent at the sliding interface rather than being spalled-off.
2) Furthermore, the load and speed were also chosen so that the test falls within the friction transition region as proposed by Souchet et al. [23] in order to better understand the lubrication mechanism rather than just wear resistance. Also, as our earlier work reported in wear [28,66,67] on the tribology of untextured MAX phases were also undertaken using these test parameters (that is, speed, load and time) and geometry, we found this useful for comparison and to help elucidate the role of laser surface texturing on the tribology of MAX phases in general rather than a specific application. Moreso, the selected test parameters in this present study will aid to understanding tribo-induced microstructures at early stages of sliding.

2.2. Laser surface texturing (LST)

First, the as-sintered sample surfaces were ground and polished to produce smooth surfaces before the laser surface texturing (LST). The texturing was performed using a continuous laser with a 1070 nm wavelength – and thus providing a Gaussian beam profile. The laser travel speed and power were set at 500 mm/s and 190 W, respectively. The distance between each laser line was 200 μm to avoid overlap. Texturing was performed in an argon atmosphere and below 200 ppm oxygen level. The direction of the laser scan was alternating for successive lines (Fig. 1(a)). The square texture on the other hand was performed in two steps. First, line scans were created which was then followed by additional line patterns perpendicular to the ones first created (Fig. 1(b)). As compared to the line textured sample, the roughness parameter of the square textured sample was considerably higher (Table 1) possibly due to the multiple laser passes required to create the eventual square pattern. Some authors have reported that deviation from smooth to rough surface could impact improved

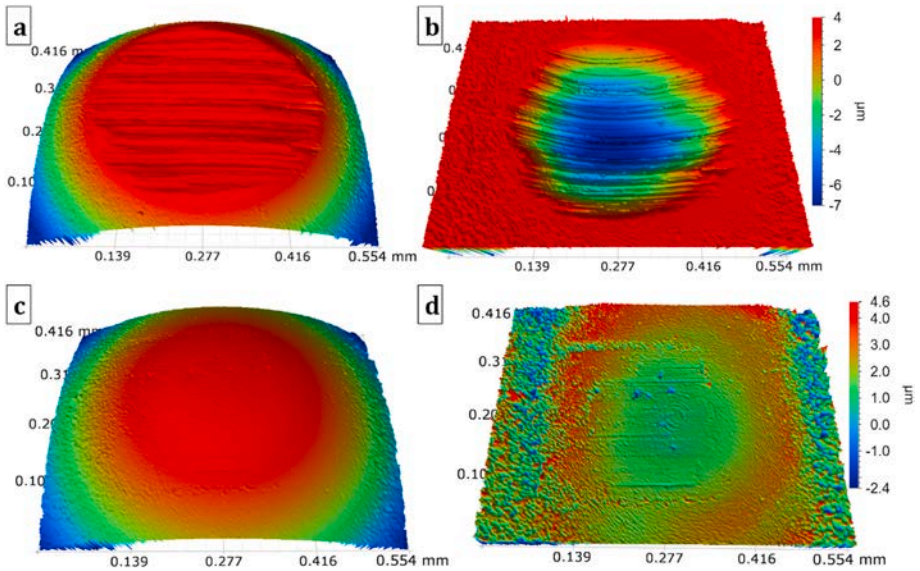

Fig. 10. 3D surface topography of the worn surface of the balls sliding against the line textured surface showing: (a–b) surface of the worn steel ball before and after sphere subtraction, and (c–d) surface of the worn alumina ball before and after sphere subtraction.

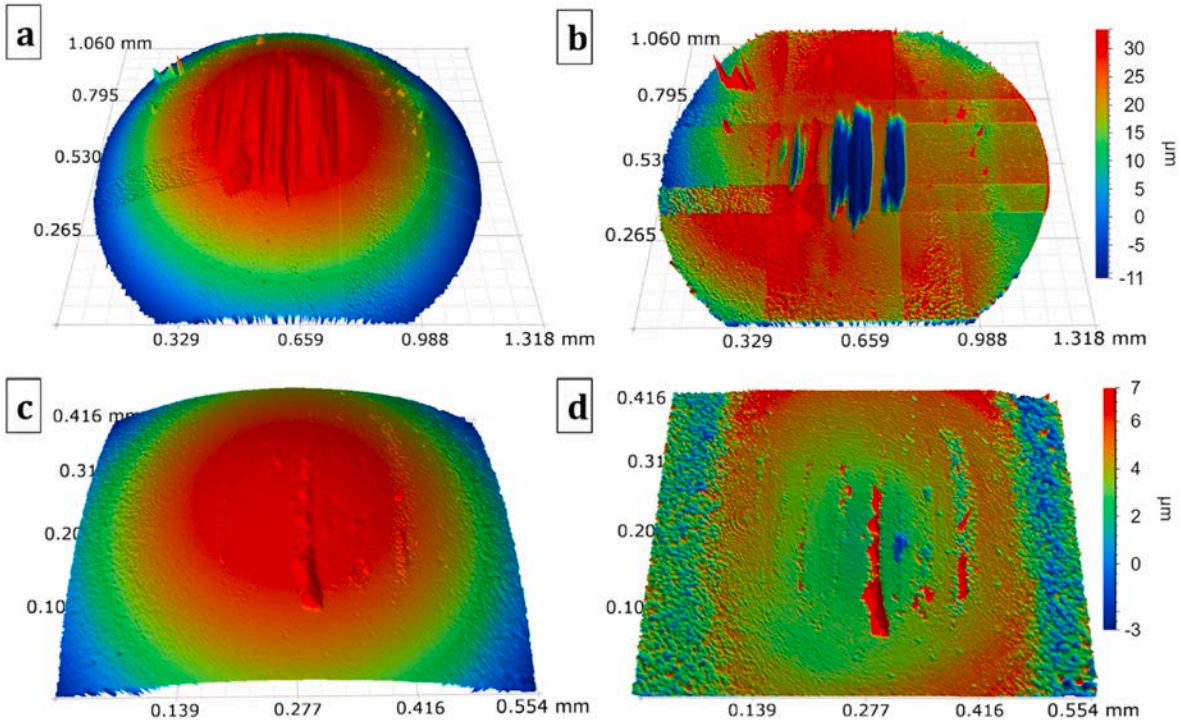

Fig. 11. 3D surface topography of the worn surface of the balls sliding against the square textured surface showing: (a–b) surface of the worn steel ball before and after sphere subtraction, and (c–d) surface of the worn alumina ball before and after sphere subtraction.

tribological properties [68,69]. According to Williams et al. [70] and Sreenath et al. [71], rough surfaces wear rapidly without seizure during running-in to promote quick conformance. Minimum initial surface roughness is necessary for quick runnin-in and only rough surfaces have a higher load carrying capacity [71].

It is important to highlight that the texture patterns created (i.e., line and square) were not chosen based on better tribological performance, but because by employing a continuous laser in contrast to a pulsed laser, it is easier to create line patterns rather than dimples and/or triangles. It was deemed unnecessary to carry out post-texturing metallographic polishing to remove the melt bulges, as previous work has shown that material bulges play a significant role in tribological

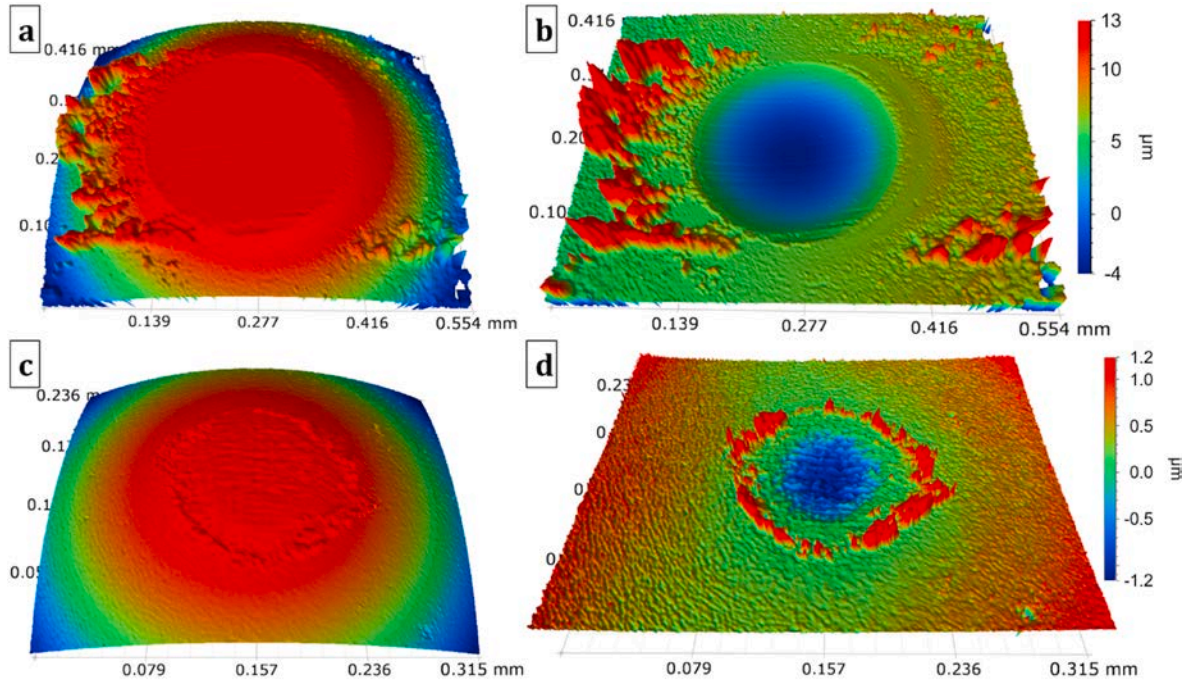

Fig. 12. 3D surface topography of the worn surface of the balls sliding against the untextured surface showing: (a–b) surface of the worn steel ball before and after sphere subtraction, and (c–d) surface of the worn alumina ball before and after sphere subtraction. Note the presence of transfer material around the worn surface.

performance of laser textured surface [46,72–74]; as they create additional lift which further decreases the contact area [75]. Also, according to Ding et al. [76], adhesion at textured surface can further be reduced by promoting the formation of micro bulges.

The actual texture density (T_d) was estimated from the SEM images using image J. The ratio of the area of the laser track (A_l) to the total area (i.e. pristine surface + laser tracks) (A_t) as shown in Fig. 2 is the texture density and was calculated using the relation:

$$T_d = \frac{A_l}{A_t} \times 100$$

Fig. 3 shows the surface topography, the line profile cross-section, and SEM images of the line textured sample. Material pileups and/or melt bulges with varying heights are evident on the sidewalls of the textured pattern; and are as a result of the laser surface remelting mechanism [75] alongside the rapid solidification due to the continuous laser employed [77]. Fig. 4 shows the surface topography, the square profile cross-section, and SEM images of the square textured sample. Also, evidence of adjacent bulges of resolidified material being pushed to the sides of the texture can be clearly seen. These observed melt bulges are due to the continuous laser employed in contrast to pico-/-femtosecond-pulses which do not yield such melt bulges [78,79]. The high magnification images of the patterns (Fig. 3(d) and Fig. 4(d)) revealed extensive microcracks following laser surface texturing. At this point it is not entirely clear which factors led to the microcracks, however, there are two important factors: (1) Owing to the laser's thermal effect (in addition to rapid heating and cooling) a large amount of molten material and residual thermal stress may result in microcracks on the textured surface; (2) Since the thermal expansion coefficient of TiC is lower than that of Ti_3SiC_2, compressive radial stresses will build up in the matrix around the TiC particles and tensile stress in the matrix upon cooling from the sintering temperature [80]. Some important texture properties (that is, texture density and depth) estimated following laser surface texturing are highlighted in Table 2. The estimated texture density is quite high, however, this may impact beneficial effects on the tribological properties of the textured sample. According to Youqiang et al. [81], high texture density gives rise to significant reduction of friction and wear of textured surfaces.

3. Results

3.1. X-ray diffraction analysis and pristine surface microstructure

Diffraction patterns showing the resultant products of the as-synthesized sample as well as the laser textured surface are shown in Fig. 5. Ti_3SiC_2 and TiC are the main products of the as-synthesized sample with some minor traces of $TiSi_2$ evident. As the scope of this work is to promote the formation of second phase TiC particles via decomposition at high sintering temperature in the Ti_3SiC_2 matrix [59], the purity of the resulting bulk sample is not of importance. The diffraction pattern of the laser textured surface on the other hand showed that the Ti_3SiC_2 phase peaks are relatively weak, and some of the peaks vanished whilst the TiC phase peaks became more intense and/or the dominant phase following laser surface texturing. Comparing the XRD patterns of the as-synthesized sample and the laser textured texture sample, the amount of TiC phase increased considerably for the laser textured sample. This is however not surprising given that the laser travel speed and the laser power employed during texturing would have brought the surface temperature (>1500 °C) [77,82,83] way above the decomposition temperature of Ti_3SiC_2. As the MAX phases do not melt but instead decompose [84] due to the sublimation of the A and/or M element as follows [85,86]:

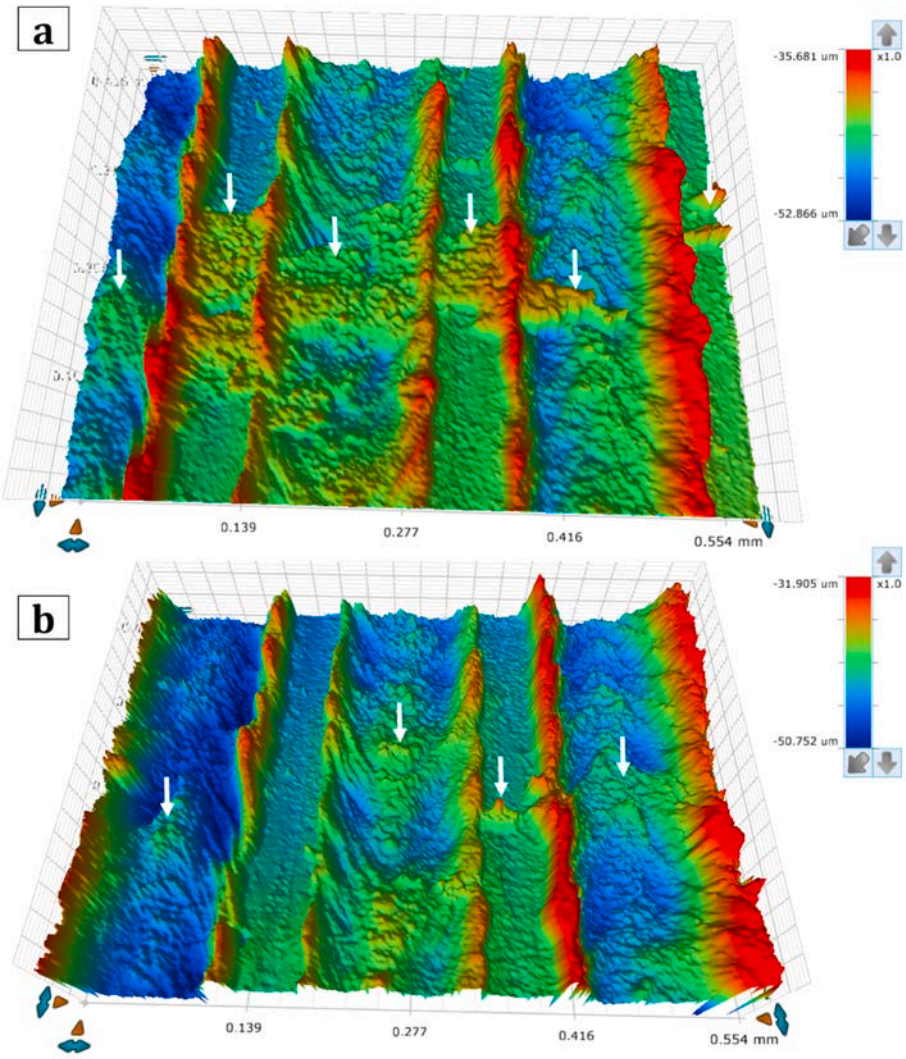

Fig. 13. 3D topography of the line textured surface wear track following sliding contact against: (a) steel and (b) alumina counterface materials. The arrows indicate wear debris in recesses.

$$M_{n+1}AX_n \rightarrow nMX + A + M$$

As the surface temperature rose above the melting point of silicon (≈1414 °C), the melting of silicon and its subsequent sublimation will bring about an inevitable phase transformation from hexagonal Ti_3SiC_2 to cubic TiC due to silicon de-intercalation as follows [85,87]:

$$Ti_3SiC_2 \rightarrow 2TiC_{(s)} + Ti_{(g)} + Si_{(g)}$$

This phase transformation occurring during the laser surface texturing led to the observed increase in the TiC phase peaks and corresponding vanishing of the Ti_3SiC_2 phase peaks. As the surface temperature during laser texturing is highest at the centre of the melt due to the Gaussian nature [77,88,89], there will be a temperature distribution at the surface [89,90], which explains why some Ti_3SiC_2 peaks remained at the textured surface; this is because the temperature might be lower at the side of the melt pool below the melting point of silicon thus preserving some Ti_3SiC_2 phase. Considering the observed phase transformation as the Ti_3SiC_2 phase do not melt but instead decompose into TiC, it is conceivable that the actual remelting during the surface texturing takes place on the TiC phase rather than the Ti_3SiC_2 phase.

The microstructure of the *as*-synthesized specimen after SPS processing is shown in Fig. 6. Two distinct phases can be clearly identified. The bright phase is the Ti_3SiC_2 whilst the dark phase is the TiC particles as confirmed by the EDS analysis (Fig. 7). Some $TiSi_2$ liquid pockets (red arrow in Fig. 6(d)) are also present. The minor silicide phase is possibly the intermediary liquid phase that has not been fully consumed during the synthesis [91,92]. This is because the growth of the Ti_3SiC_2 phase takes place within the $TiSi_2$ liquid following the dissolution of the Ti–C nuclei in the Ti–Si melt, thus the precipitation of layered Ti_3SiC_2 [91]. The TiC particles appear to be inhomogeneously distributed in the Ti_3SiC_2 matrix. In some regions they are homogeneously distributed (Fig. 6(c)) whilst in other regions they form clusters (Fig. 6(a – b)). The differential distribution of TiC particles in the Ti_3SiC_2 matrix is most likely a result of being produced in situ as an ancillary phase rather than being a bulk addition. Also, it appears that abnormal Ti_3SiC_2 grain growth occurs in areas where the concentration of TiC is minimal [92,93]. Further details on microstructural development can be found in our earlier work [59,94].

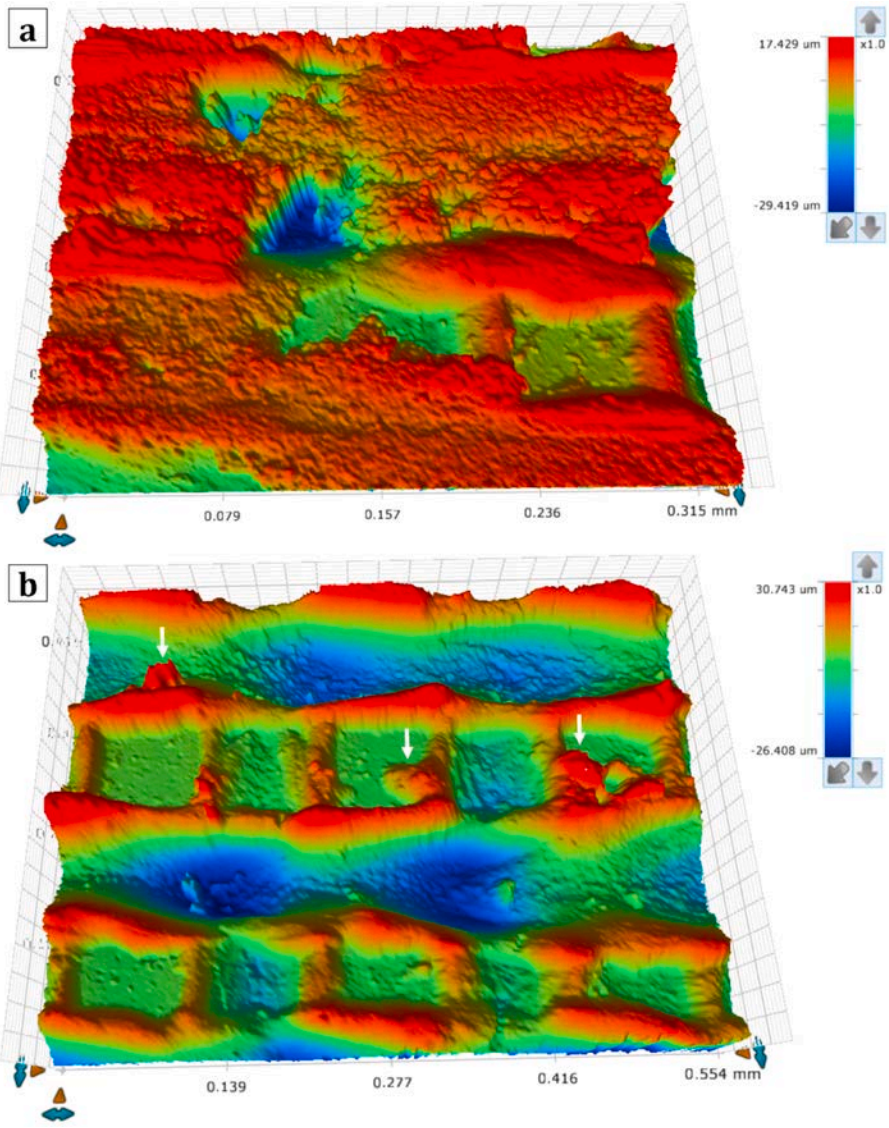

Fig. 14. 3D topography of the square textured surface wear track following sliding contact against: (a) steel and (b) alumina counterface materials. The arrows indicate wear debris in recesses.

3.2. Density and vickers hardness measurement

In general, the synthesized SPSed disc was fully dense with relative density in excess of 99% upon taking into account all the phases in the bulk sample. According to the Vickers hardness result, a significant difference in hardness was observed for the pristine (untextured) and textured SPSed surfaces. After laser texturing, the Vickers hardness of the line and squared-textured discs increased by 450% (from 704.6 HV untextured to 3878.3 HV). The enhancement in hardness can be attributed to the possible phase transformation induced during laser surface texturing [95–98]. The heat generated during laser surface texturing is high enough to bring about transformation from hexagonal Ti_3SiC_2 to cubic TiC_x due to the de-intercalation of Si and its subsequent evaporation [87,99,100] in consistent with the diffraction pattern in Fig. 5.

3.3. Evolution of friction coefficient

Figs. 8 and 9 compare the evolution of friction coefficient as a function of sliding time for pristine (untextured) surface and textured surfaces during dry sliding at room temperature against the hardened steel and alumina counterbodies respectively. In general, the friction coefficient of the textured surfaces was lower and stable in comparison to the untextured surface against both the steel counterface (Fig. 8) and alumina counterface (Fig. 9). Similar observation have been reported elsewhere for the laser textured surface [48,101,102]. For the tests against steel, it can be seen that at the early stage of sliding (i.e. run-in stage), the friction coefficient of the textured samples was initially higher in contrast to the untextured surface. The high run-in friction coefficient can be attributed directly to the high surface roughness of the textured specimens as well as possible high energy barrier induced by the bulges [103,104]. However, the transition from running-in

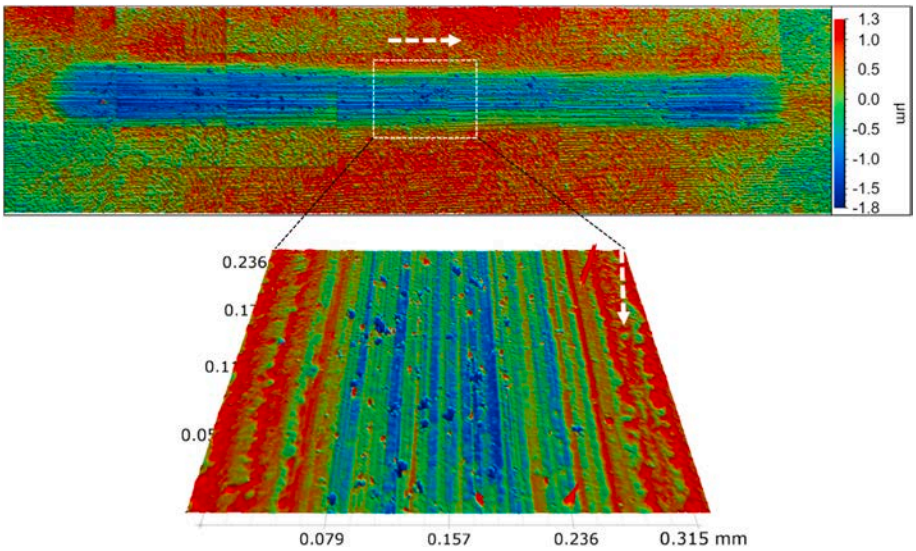

Fig. 15(a). 3D topography of the wear track generated on the untextured surface following sliding contact against the steel counterface.

(high-friction) to steady-state (low-friction) friction took place rapidly for the textured samples, whilst for the untextured sample, the steady state friction was higher as the sliding time increases. Rapid transition from run-in to steady state friction have been reported for laser textured specimen by investigators [45,81,103]. It seems that the increase in contact pressure at the texture edges and/or bulges led to the activation of tribofilms via stress-induced tribochemical reactions which reduced friction – and thus the observed instantaneous friction transition [105]. Also, it is conceivable that the rapid deformation taking place at asperity contact due to the high contact stress induced by the low contact area may also play a role in expediting the transition to steady-state friction for the textured specimen [103]. Moreso, the stable friction can be correlated directly to the entrapment of wear debris by the recesses – and thus removing them from the sliding interface [40]. Entrapment of the wear debris reduced the growth and subsequent agglomeration of the wear particles, thus reducing ploughing of the textured surface [39, 106]. However, the untextured sample showed a large fluctuation of friction coefficient which continually increased in the steady state regime. The observed fluctuation and increased friction coefficient can be directly correlated to the initial adhesion effects at the sliding surface which serves a prerequisite to increased sliding contact area, fracture, and wear debris generation [103].

For the test against the alumina ball, the initial starting run-in friction was considerably higher for the untextured surface. The friction rose rapidly for the first ~500s of sliding, but then fell, becoming stable after ~1500s at a friction coefficient of ~0.35. Such a friction transition has been linked to the intrinsic lubricating mechanism in MAX phases [20,23]. For the textured surface, similar to observation of the sliding test against steel, abrupt transition from run-in to steady state friction can be clearly seen. Furthermore, the steady state friction coefficient of the square textured surface was considerable lower than the line textured surface. In general, the friction coefficient of the textured surface was lower and more stable in contrast to the untextured surface. Comparing the friction evolution of the untextured surface following

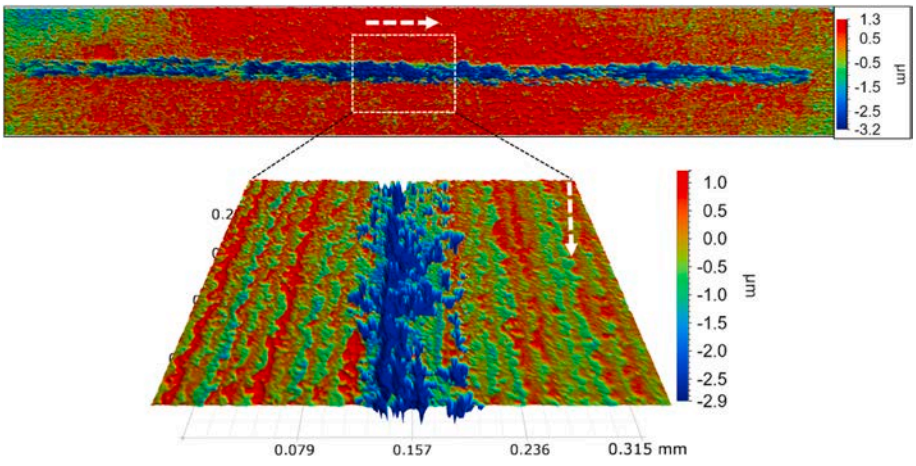

Fig. 15(b). 3D topography of the wear track generated on the untextured surface following sliding contact against the alumina counterface.

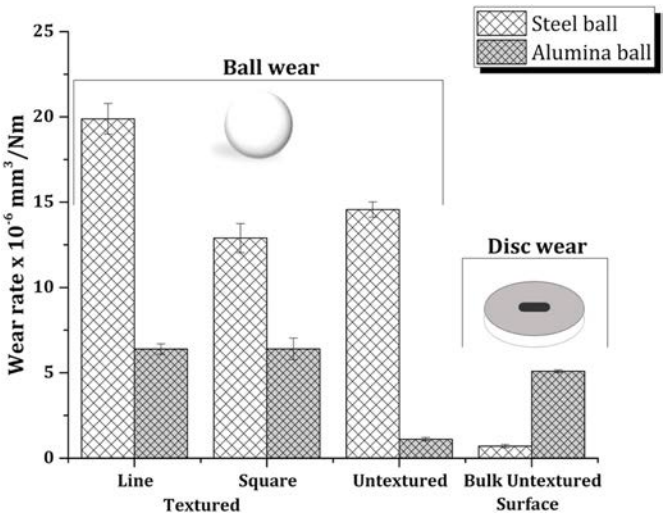

Fig. 16. Comparative wear rate plots of the balls (steel and alumina) after sliding against the textured and untextured MAX phase material surface as well as the wear rate of the untextured MAX phase surface (disc) after sliding against the steel and alumina counterbodies. Note: the wear rate of the textured discs could not be estimated due to absence of wear scar.

sliding contact against the steel and the alumina counterbodies, it is clear that the steady state friction for the test against alumina was more stable and lower with only intermittent fluctuation. The differences in friction evolution may due to the increased wear debris generation and subsequent agglomeration at the sliding interface for the test against steel counterbody [106].

3.4. Worn surface analysis of the tribopairs

3.4.1. 3D optical images of the worn tribopairs

Figs. 10 – 12 shows the 3D optical topography images of the wear scar developed on the counterface, that is, the steel and Al_2O_3 balls following the sliding friction and wear tests against the line textured (Fig. 10), square textured (Fig. 11), and the untextured surfaces (Fig. 12), respectively. In general, the wear of the ball was found to be lowest for the tests against the untextured sample, which might be due to a possible correlation between surface roughness and wear [45]. For the LST samples, the observed wear scars on the steel ball was much more pronounced as compared to the alumina ball [76,107], with the extent of wear higher for the line textured sample albeit lower surface roughness. This may be correlated directly to the further reduction in contact area for the square textured surface due to the increase in bulge height [73,76]. Comparing the wear of the steel and alumina ball after sliding against the untextured surface, it can be seen that the wear of the steel ball was much more significant, with only little wear observed on the surface of the alumina ball. This observation is however not surprising as it correlates well with the friction evolution; and this may be linked to the lower hardness of the steel ball as compared to alumina. Moreso, it is also possible that the incipient tribofilm formation at the sliding interface during the sliding contact against alumina counterface shielded the surface of the ball [20,108].

Figs. 13 – 15 shows the 3D surface topography of the sliding track generated on the textured and untextured MAX phase material following dry-sliding contact against steel and alumina counterbodies. The topography of the line surface textured MAX phase material after sliding against steel (Fig. 13(a)) and alumina (Fig. 13(b)) counterbodies is presented in Fig. 13. As shown, the line texture pattern appears to be relatively intact with little or no wear of the bulges. However, evidence of wear debris (generated from the counterface) entrapment inside the grooves (white arrows) was found, particularly for the sliding test against steel counterface [107,109]. Fig. 14 shows the wear track on the square surface textured MAX phase material following sliding contact against steel (Fig. 14(a)) and alumina (Fig. 14(b)). As shown in Fig. 14 (a), the square texture is completely filled with counterface material following severe wear and consequent transfer of the steel ball wear debris onto the sliding surface. The recesses in the square patterns effectively act as a wear debris reservoir by collecting and trapping the debris below the sliding interface [39,81,110], thus preventing them from acting as abrasive third-bodies [39,110]. Similarly, evidence of wear debris entrapment (white arrow (Fig. 14(b)) can be seen for the test against alumina ball albeit the amount of transfer material was small due to minimal wear of the alumina counterface [20]. In general wear was confined to the melt bulges that accompany the laser textured patterns as the applied load was supported solely by the melt bulges thus preventing counterface contact with the ground surface [73,75]. Conversely, preferential wear of the counterbody material (steel and alumina) due to their low hardness in comparison with the melt bulge (that is, mainly TiC) was observed [103].

Fig. 15 shows the 3D topography of the wear track generated on the untextured MAX phase material surface after sliding contact against the counterbodies. The wear track appears to be wider and shallow for the test against steel counterface (Fig. 15(a)) in contrast to the narrow and deep track generated with the test against alumina counterface (Fig. 15 (b)). It is not surprising that the width of the track is wider against the steel counterface given the extent at which the steel ball was worn (Fig. 12(a – b)), as such, the contact area on the bulk material will increase as a function of time [45]. Fig. 16 shows the comparative wear rate plot of the balls (steel and alumina) after sliding against the textured (line and square) and untextured surfaces as well as the wear rate of the untextured MAX phase material disc after sliding against steel and alumina counterfaces.

3.4.2. SEM micrographs of the worn bulk samples

Figs. 17 – 22 show secondary electron (SE) SEM images obtained from the textured (square and line) and the untextured surfaces tested against the steel and alumina counterbodies. Fig. 17 shows the worn surface of the square textured MAX phase material after sliding against the steel counterbody. The majority of the recesses in the square texture at the centre of the wear track are fully filled with wear debris from the steel counterpart (Fig. 17(a – b)), and in some regions wear debris are smeared into the laser channel (Fig. 17(c)) once the square recesses become completely filled. A closer look at the SEM image showed that the steel counterface had made contact with the trailing edge of the square pattern (evident as micro-ploughing Fig. 17(d)), and this suggest that there was mild wear of the bulges in certain regions consistent with observations reported elsewhere [75,76]. Fig. 17(e) shows the contact points on the textured surface (red arrows), and a high magnification image of a contact point (Fig. 17(f)) revealed evidence of surface smoothening; thus suggesting the presence of what seems to be a sintered tribofilm at the sliding interface [111,112]. In addition, there was local evidence of stick-slip type behaviour in the trailing edge of the tribofilm. Fig. 18 shows the worn surface of the square textured MAX phase material after sliding against the alumina counterface. Evidence of wear debris can be seen in the recesses in the square patterns and along the laser channel (Fig. 18(a – c)) albeit smaller in comparison to the steel

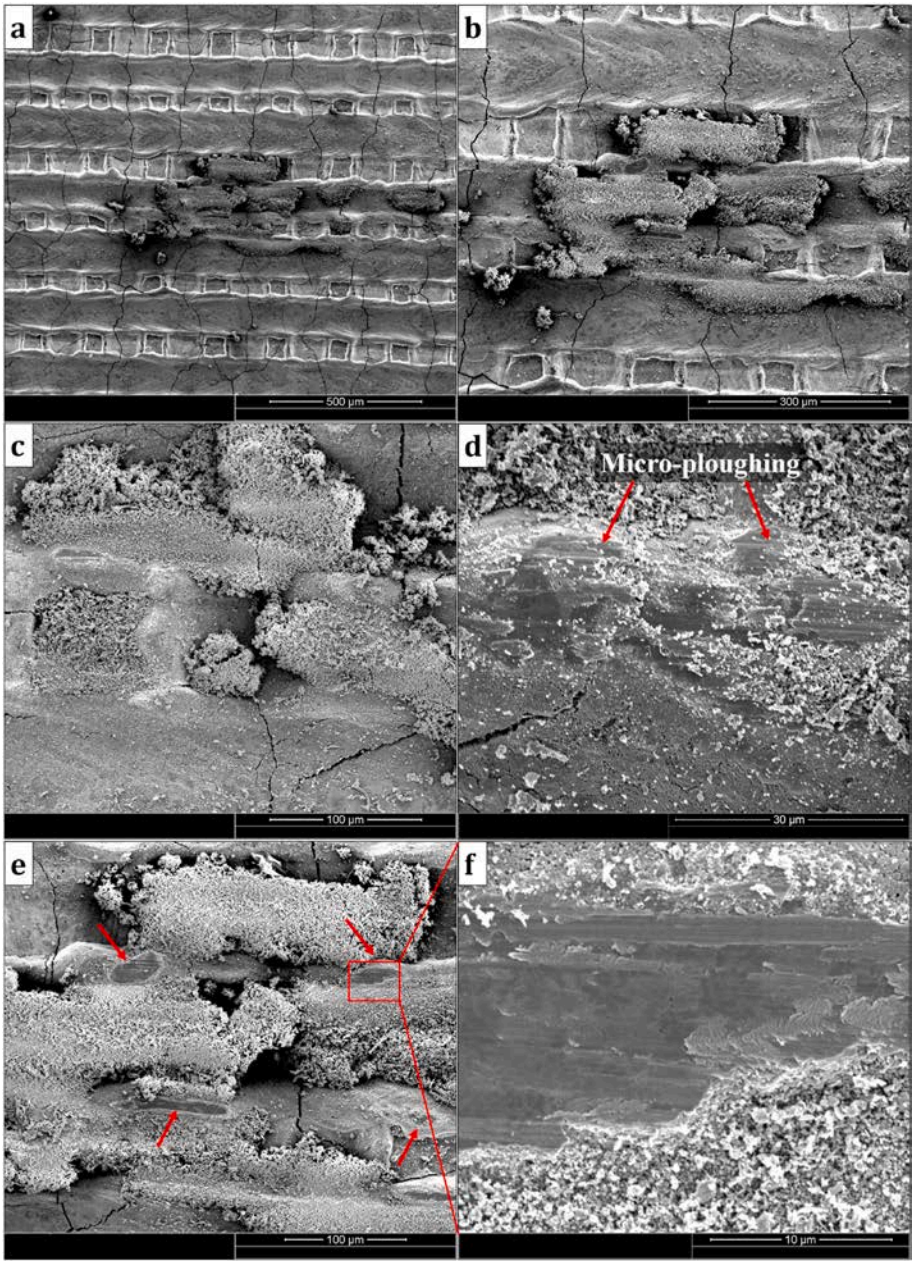

Fig. 17. SEM images of the worn surface of the square textured MAX phase material after dry-sliding against steel counterface showing: (a–b) low and high magnification images of wear debris entrapment inside the square-textured pattern, (c) evidence of wear debris smeared unto the laser channel once the square microcavities get completely filled, (d) mild micro-ploughing at contact points with the edge of the pattern, (e) sliding contact points on textured surface, and (f) high magnification image of highlighted contact point in (e) revealing surface smoothening effect due to tribo-sintering of the supplied particles on the sliding surface.

counterbody due to minimal wear. The tribofilm appeared to comprise of compacted wear debris, and also the evidence of surface smoothening further indicates possible contact between the alumina ball and the trailing edge of the square pattern (Fig. 18(d)). There was no sign of stick-slip type behaviour in the tribofilm produced against the alumina ball, suggesting a possible difference in tribofilm chemistry. In general, the underlying pristine MAX phase material beneath the textured surface (Fig. 18(e – f)) remained intact albeit texture-induced microcracking.

The worn surface following sliding contact between the line textured surface and the steel counterbody is shown in Fig. 19. The presence of thin transfer film (Fig. 19(a – c)) sheared across the contact points is clearly evident. Furthermore, some transfer material from the steel counterface can also be seen in the wear track (Fig. 19(d)). Fig. 20 shows the wear track of the line textured surface after sliding against the alumina counterbody. Evidence of contact between the two surfaces as well as transfer material (Fig. 20(a – b)) from the alumina ball along the laser channel can be seen. High magnification images taken from the contact point made with the trailing edge of the line texture (Fig. 20(c – d)) by the alumina ball also revealed evidence of surface smoothening and sheared tribofilm.

In contrast to the wear track generated on the textured surface where little or no visible contact impression was seen on the bulk sample other than traces of wear debris, a distinct bulk material removal was evident on the untextured contact surface. This made it possible to estimate the wear rate of the untextured bulk MAX phase composite even though this

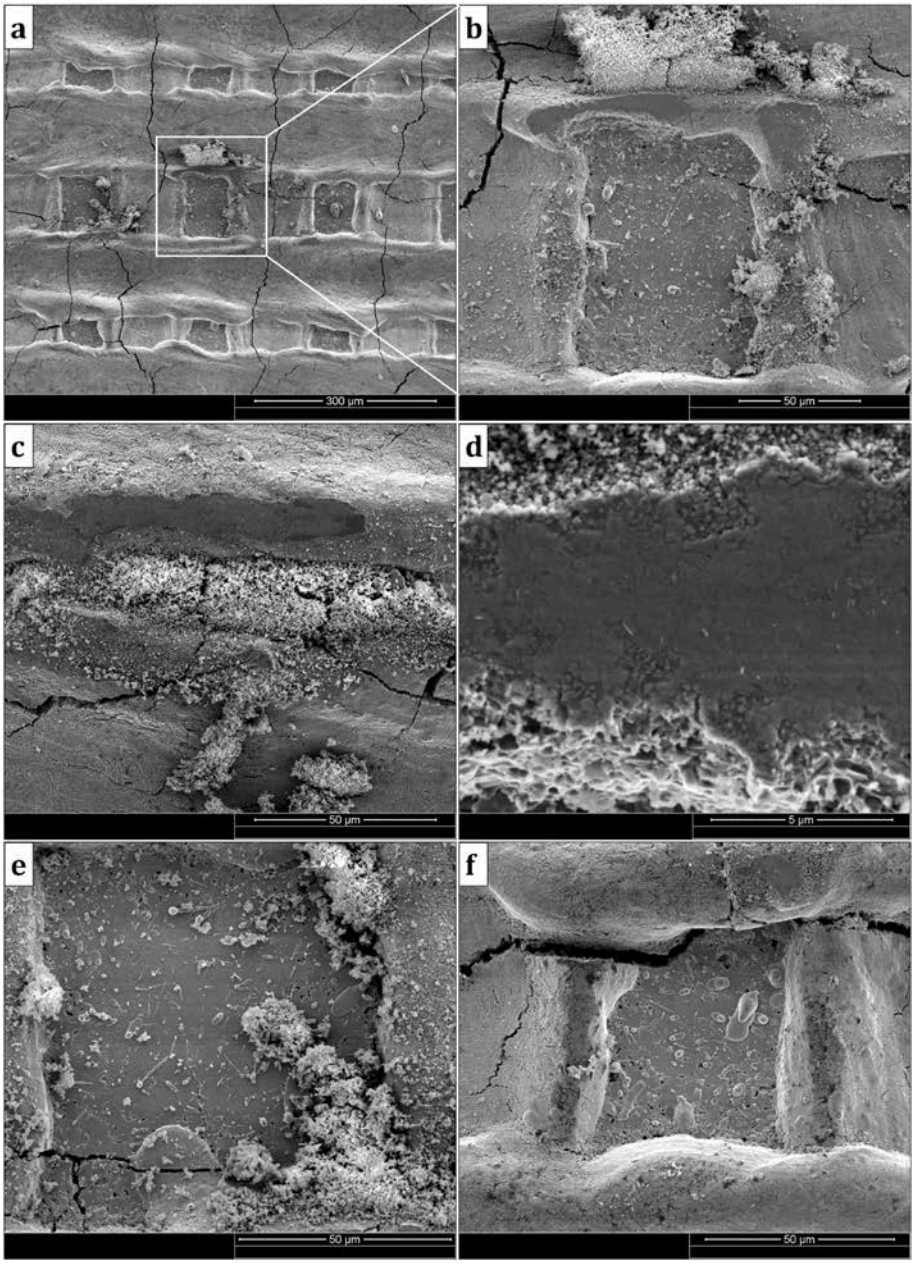

Fig. 18. SEM images of the worn surface of the square textured MAX phase material after dry sliding against alumina counterface showing: (a) wear debris generation and subsequent entrapment within the laser microcavities, (b) high magnification of a section in (a), (c) evidence of contact point and smeared wear debris along the laser channel, (d) surface smoothening at sliding interface and (e–f) reveals that the underlying surface of the MAX phase material beneath the texture remained intact.

was not possible with the textured bulk surfaces. Fig. 21 displays the micrographs of the worn surface of the untextured surface after dry-sliding contact against the steel counterface. Evidence of mild and diffuse damage spots can be seen inside the wear track from the low magnification image of a section from the track length (Fig. 21(a)). High magnification image of these damage spots revealed the extent of the grain damage (Fig. 21(b)) and the onset of grain pull-out (Fig. 21(c)), surface grain fracture and grain delamination (Fig. 21(d)), as well as evidence of pores left behind following grain pull-out, which acted as a reservoir (Fig. 21(e)) for wear debris. Also, wear fragments most likely from the steel counterface appears to have been oxidized and compacted on the sliding interface (Fig. 21(f)), thus constituting a tribological layer. It is noteworthy to point out that the MAX grains in the surrounding of the TiC particles appeared relatively intact in contrast to regions where there are no TiC particles in matrix as evident in Fig. 21(d). It is plausible that the TiC particles provided a pinning effect on the Ti_3SiC_2 grains; and this is consistent with observations reported elsewhere [33].

On the other hand, extensive and concentrated grain damage can be clearly seen from the low magnification image obtained from a section of the untextured surface worn track length after dry-sliding contact against alumina counterface (Fig. 22(a)). High magnification images taken from the damage spots revealed excessive grain damage as well as transgranular fracture within the grains (Fig. 22(b)). The pits left behind following grain pull-out and the fracture of the surface grains (Fig. 22(c – d)) entrapped the some of the wear particles, thus reducing the wear fragments in the tribological system. Similar wear debris entrapment

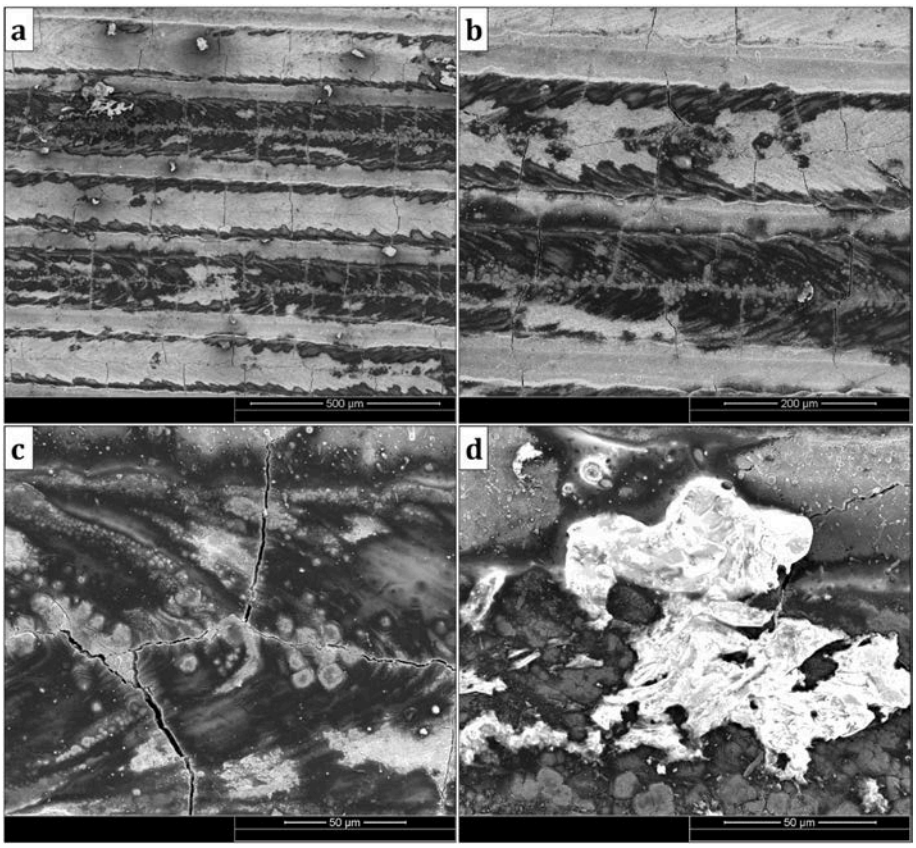

Fig. 19. SEM images of the worn surface of the line textured MAX phase material after dry-sliding against steel counterface showing: (a) wear debris and thin layer of surface films at the sliding interface, (b) high magnification of a section from (a), (c) evenly sheared thin-layer surface film at the sliding interface and (d) transfer steel wear particle inside the laser channel.

behaviour in porous samples has been reported elsewhere [113]. Furthermore, there was evidence of possible sintering of the wear debris, thus leading to a protective glaze (Fig. 22(e – f)) dispersed inside the wear track. Some of the glazed layer seems to have been detached and/or fracture orthogonally to the sliding direction (Fig. 22(e)) possibly after reaching a certain thickness. Comparing the worn surface of the untextured surface upon sliding against the steel and alumina counterbodies, it is clear the extent of grain damage is much more significant for the sliding test against alumina counterface. Albeit the high steady state friction for the test against the steel, the damage to the worn surface was minimal. This further supports the initial assumption that the oxidation of the Fe wear particles at the sliding interface played a vital role in shielding the bulk surface from extensive deformation by absorbing some of the contact load as well as lubricating the sliding interface [112].

3.5. Raman analysis of friction contact regions

In order to further understand the role of tribo-oxidation and/or intrinsic lubrication on the friction and wear behaviour, Raman analysis of the evolved surface chemistry was undertaken. For the square textured surface, the evolved surface chemistry following sliding contact against steel (Fig. 23) consisted of mainly hematite (Fe_2O_3) [114,115] and some traces of the G-band of graphitic carbon [116,117]. Against the alumina counterface, the surface chemistry (Fig. 23) was mainly titanium oxycarbide (TiO_xC_y) [118] as well as traces of the G-band of graphitic carbon. For the line textured surface, the evolved surface chemistry following sliding contact against steel (Fig. 24) consisted of solely hematite. However, following repeated Raman scans of the same wear track, an area consisting of essentially graphitic carbon was found (Fig. 25); this highlights the complex nature of the evolved surface chemistry architecture. It is plausible that most of the graphitic carbon forming intrinsically from the breakdown of the MAX phase have been covered by subsequent tribofilm formed by the compaction of wear debris and/or possibly worn off. Against the alumina counterface (Fig. 24), the line textured worn surface chemistry consisted of both titanium oxycarbide (TiO_xC_y) and graphitic carbon. On the other hand, for the untextured surface, the evolved chemistry in the wear track upon sliding contact against steel counterface (Fig. 26) consisted of mainly hematite (Fe_2O_3) and some traces of G-band of graphitic carbon. In contrast, against the alumina counterface (Fig. 26), the chemistry of the worn surface consisted of both anatase (TiO_2) [119] and graphitic carbon.

4. Discussion

Depending on the counterbody, two different running-in and steady state friction behaviours were observed. According to Ding et al. [76] surface adhesion force is dependent on the surface activity and the real contact area. As the apparent area of contact are similar under the same

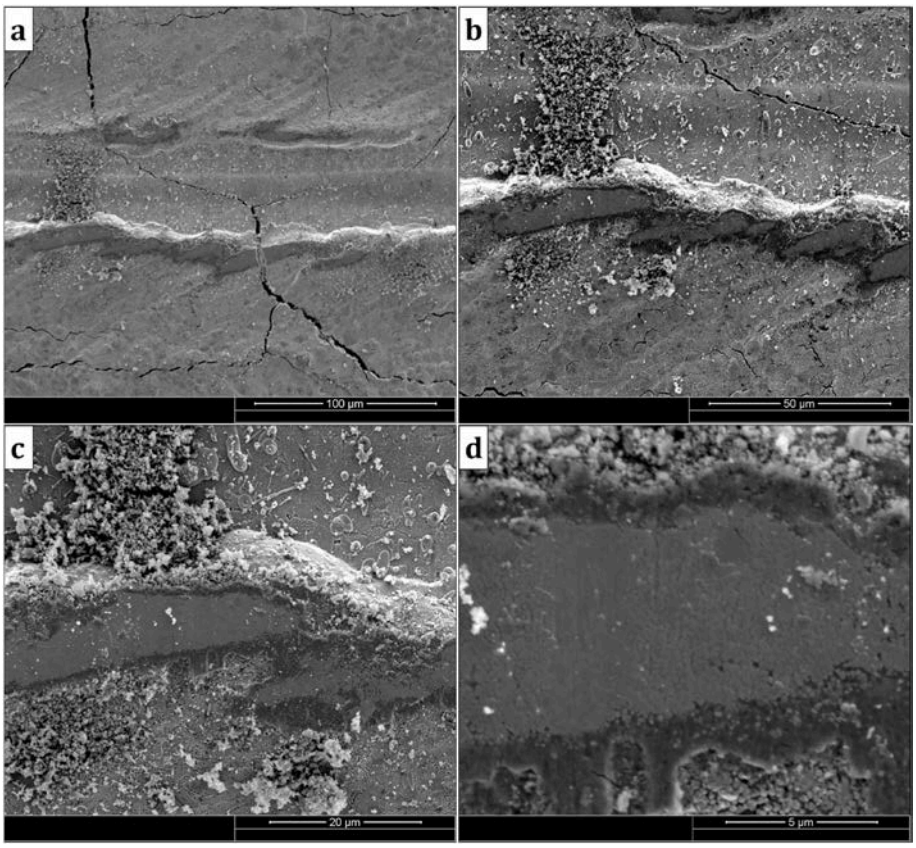

Fig. 20. SEM images of the worn surface of the line textured MAX phase material after dry-sliding against alumina counterface showing: (a) contact points and wear debris entrapment in the laser channel, (b) high magnification image taken from (a), (c) smoothening effect at contact points and (d) higher magnification of (c) further revealing the lubricity at the sliding interface.

load for the steel and alumina counterbodies when sliding against the textured and untextured surfaces, it is plausible that the surface activity and hardness of the counterbodies [107,109] also influenced the friction behaviour. Since the surface activity of the alumina ball is inert in contrast to the hardened steel ball, it is probable that the observed dissimilarities in friction evolution could be linked directly to the differences in surface activity [76], excluding possible plastic deformation on the contact surface. In addition, compared with the hardness of the Al_2O_3 ball, the hardness of the steel ball is lower; this will result in more Fe particles due to abrasive wear at the sliding interface [107]. However, as the wear of the steel ball led to increased Fe wear debris generation and its subsequent oxidation to Fe_2O_3 during the sliding process; the compaction of this tribofilm at the sliding interface will shield the bulk sample from severe wear [120,121].

The fundamental differences in the wear behaviour of the different surface structures (that is, textured and untextured) is linked to the recesses in the textured surface that helped reduce the contact area, thereby providing a discontinuous sliding surface that does not favour adhesion of the tribopairs [122,123] as well as the evolved microstructure of the textured surface [124]. As third-body abrasive wear linked to wear debris generation at the sliding interface – this leads to grain pullout and fracture – has often been reported as the dominant wear mechanism of Ti_3SiC_2 [20,23], the surface texture helped reduce adhesion and trapped wear fragments detached at the asperity contact [39,56]. Further, whilst the line and square texture patterns led to significant improvement in friction and wear, it is clear that the square textured pattern performed better judging from the friction evolution. This can be correlated directly to further reduction in contact area as compared to the line textured surface. Similar observation has been reported elsewhere for square patterns [125–128].

Besides the role of the texture as a wear debris trap, reduction in contact area as well as reducing the adhesion of the tribopairs, the evolved microstructure at the textured surface played a significant role in reducing the friction and wear. Similar laser surface texture-induced phase transformation leading to hardening at textured surface has been reported by investigators [88,97,105]. The increase in surface hardness due to TiC formation means that the bulk sample is harder than the ball counterpart – and this implies that during sliding, the counterface will wear preferentially. Also, the increase in surface hardness means that most of the applied load is supported at the surface leading to small contact area due to its mechanical strength [40,103]. It is noteworthy that the observed microcracking following the surface texturing did not appear to play any role in the friction and wear. This is partly because the sliding action was confined to the surface bulge and/or textured region whilst the microcrack underneath was completely shielded from the sliding action. It is unclear at this time what the case would be when the surface bulges are completely worn off at longer sliding times and contact is made directly with the pristine surface.

An important aspect of laser surface texturing that plays a significant role in friction and wear properties but often overlooked is residual

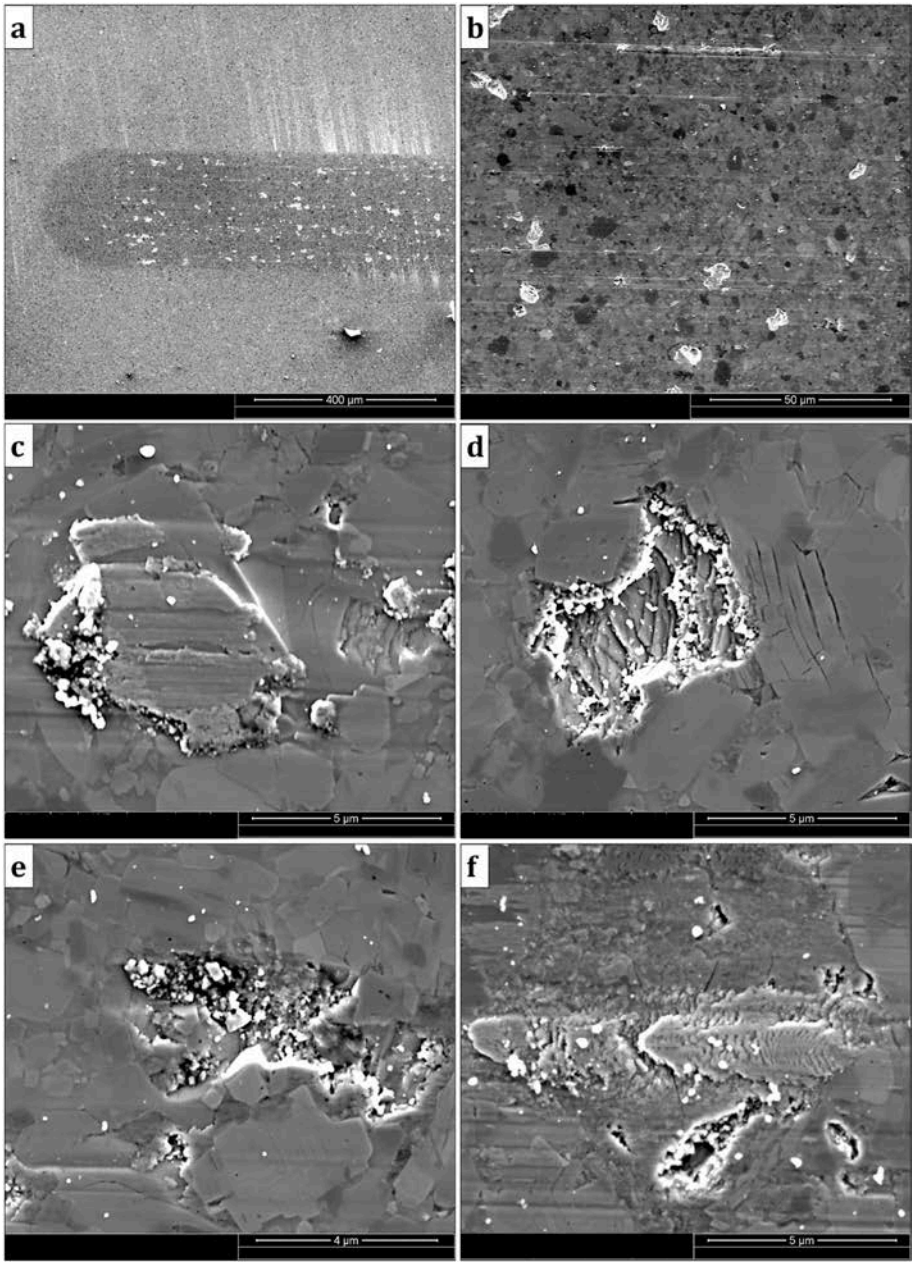

Fig. 21. SEM images of the worn surface of the untextured MAX phase material after dry-sliding against steel counterface showing: (a) a section of the track length revealing diffuse damage spots, (b–c) a high magnification image of the damage spots in (a) showing the onset of grain pull-out (Fig. 21(c)), (d) fracture of surface grains and grain delamination, (e) pits left behind after grain pull-out acting as reservoir for wear particles, and (f) tribolayer formed due to oxidation and compaction of transferred steel particles.

stress [129]. Laser surface texturing is known to generate compressive residual stresses and high density arrays of dislocation mainly by thermal stress due to the high temperature employed during texturing [69]. Compressive residual stress improves wear performance and its magnitude increases with increasing number of laser passes [95]. In effect, it is plausible that the incipient stress on the surface during the sliding action is counteracted by those generated following laser texturing – and this further provides a surface protection [95].

For the untextured surface, it was clearly evident that Ti_3SiC_2 grain pullout in areas of the matrix without TiC particles was pronounced. This further highlights the role of increased contact area and adhesion on the ease of Ti_3SiC_2 grain pullouts. Whilst the TiC particles appeared to have a pinning effect on the Ti_3SiC_2 grains [84], the fact that they are not distributed homogeneously in the Ti_3SiC_2 matrix – as they are formed in situ [84] – implies that a large section of the Ti_3SiC_2 grains are without the protection of the TiC particles. One way to mitigate this is to add TiC particles as a bulk addition in the starting powder mixture – this will aid in the homogeneous distribution of the TiC particles in the Ti_3SiC_2 matrix.

Irrespective of the different surface structure (that is, textured and untextured), the dominant wear mechanism for the sliding conditions employed in this study is tribo-oxidation. Owing to the dry sliding condition, the surface temperature at the asperity contact is high enough to promote the oxidation of the wear particles generated [130]. As evidenced in this study, some wear fragments generated at asperity contact and/or by adhesion of tribopairs are in some cases trapped

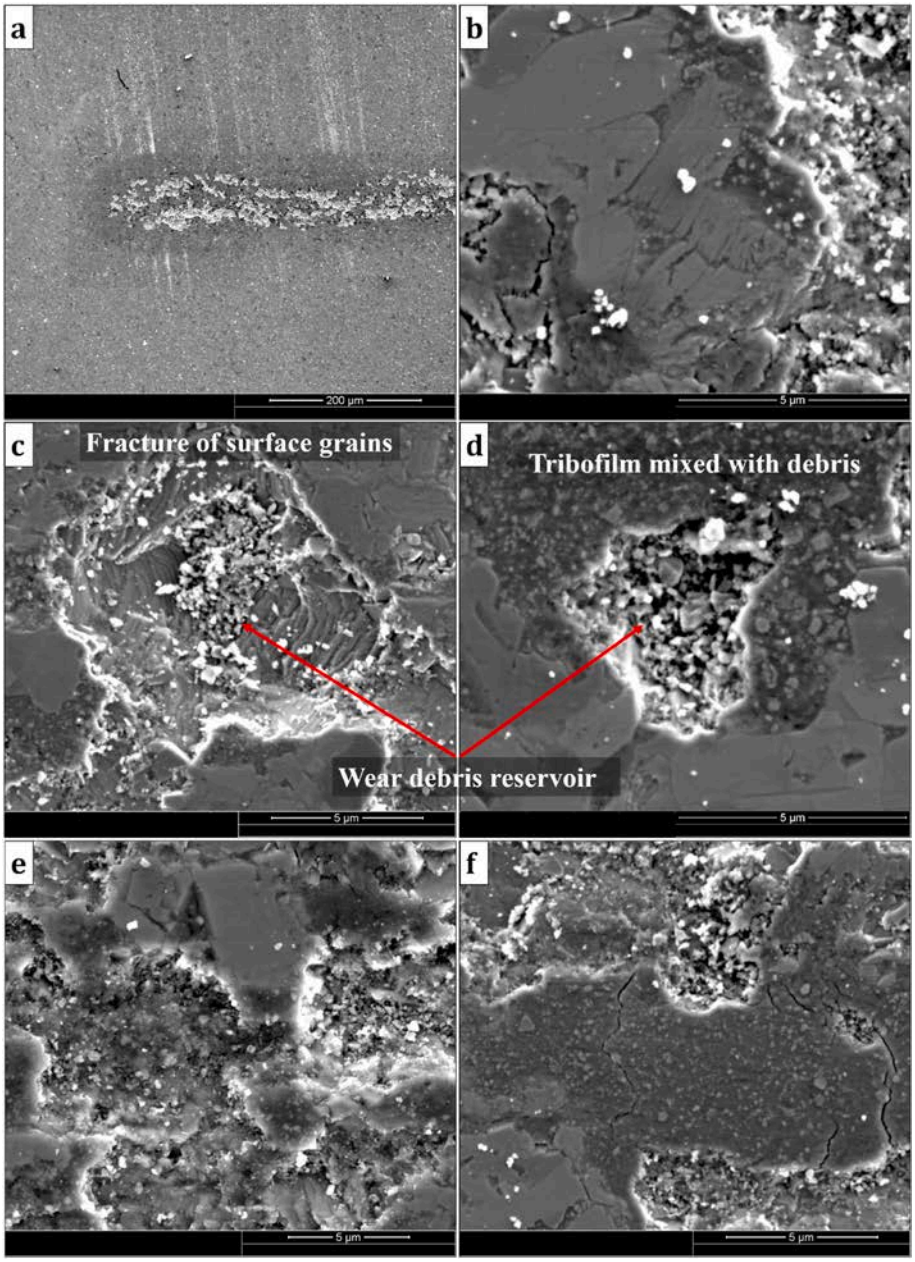

Fig. 22. SEM images of the worn surface of the untextured MAX phase material after dry-sliding against alumina counterface showing: (a) a section of the track length revealing extensive and concentrated damage spots, (b) high magnification image taken from the damage spot showing severe grain delamination, fracture and pulverization, (c) fracture of surface grains, (d) pits left behind after grain pull-out acting as reservoir for wear particles and (e–f) evidence of scale-sintered tribolayer formation and detachment.

between the mating surfaces. These wear particles are then strain-hardened following repeated attrition and oxidized (oxidation is activated due to increase in surface area by wear debris generation and frictional heat) [131]. This led to oxidized nanoparticles such as Fe_2O_3, TiO_2 and TiO_xC_y at the sliding surface as a function of the counterface material. These oxidized nanoparticles are agglomerated into a tribological layer which in some cases sinter to form a protective glaze layer that supports the applied load [132].

5. Conclusions

Laser surface texturing was successfully employed to create line and square-type microtextures in order to improve the tribological properties of MAX phase composite of the type Ti_3SiC_2–TiC. The friction and wear behaviour of the textured and untextured bulk samples was investigated using different counterbodies. The role of texture and lubrication mechanism(s) are therefore elucidated as follows:

- Laser texture was effective in improving the friction and wear of the MAX phase material by reducing the area of contact, entrapping wear debris as well as creating surface hardening effect induced by phase transformation. In general, an excessive steel transfer layer was formed, while the alumina led to much less transfer on all the worn surfaces.

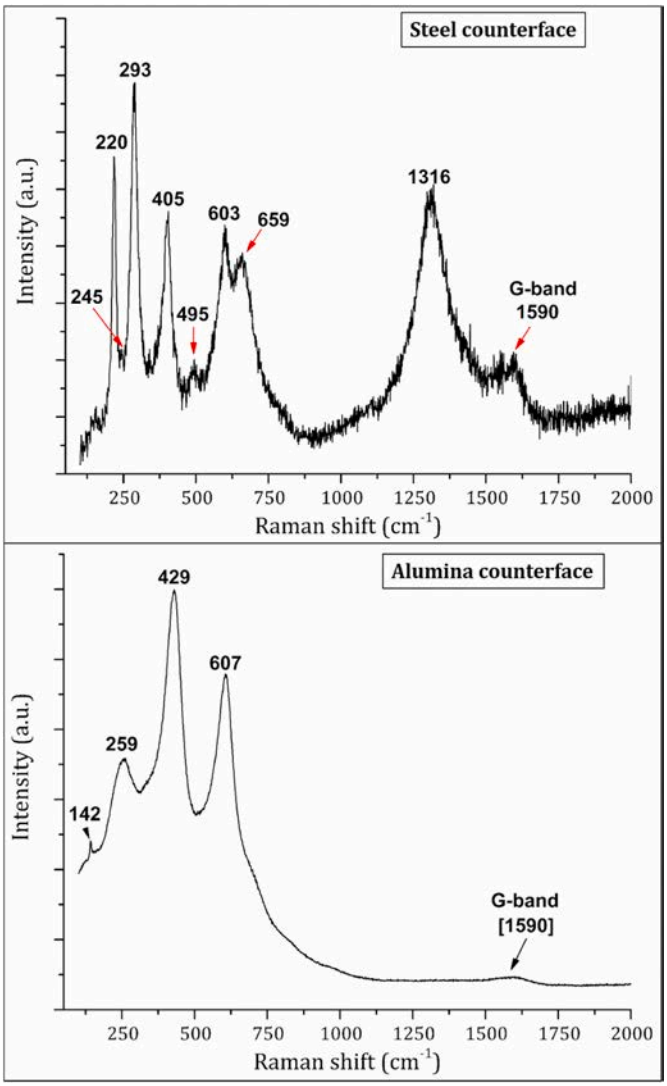

Fig. 23. Evolution of surface chemistry following dry-sliding contact between the square textured MAX phase material against the steel and alumina counterfaces.

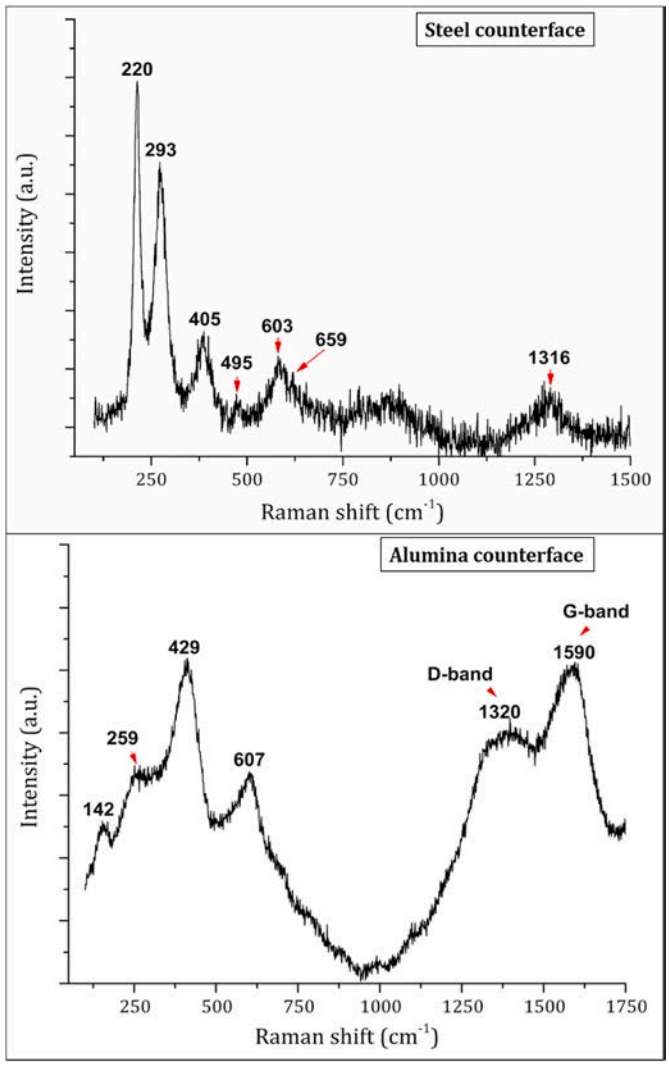

Fig. 24. Evolution of surface chemistry following dry-sliding contact between the line textured MAX phase material against the steel and alumina counterfaces.

- Melt bulges left behind following laser surface texturing plays a significant role in wear behaviour by creating surface lift thereby further reducing the contact.
- The non-textured surface exhibited severe adhesive wear, grain pull-out, and high friction during the running-in period (most especially against alumina counterface). In contrast, laser textured surface yielded a constant, low friction with little or no wear of the underlying microtextures – as wear was limited to the periphery of the texture.
- Surface texturing led to accelerated wear of the counterbodies and could be beneficial if quick running-in is desired and accelerated wear on the counterface is acceptable.
- Synergistic interplay of texture, topography and microstructure evolution led to improved frictional and wear for the test condition (s) employed.

Author agreement

We confirm that the manuscript has been read and approved by all named authors and that there are no other persons who satisfied the criteria for authorship but are not listed. We further confirm that the order of authors listed in the manuscript has been approved by all of us.

We confirm that we have given due consideration to the protection of intellectual property associated with this work and that there are no impediments to publication, including the timing of publication, with respect to intellectual property. In so doing we confirm that we have followed the regulations of our institutions concerning intellectual property.

Declaration of competing interest

The authors declare that they have no known competing financial interests or personal relationships that could have appeared to influence the work reported in this paper.

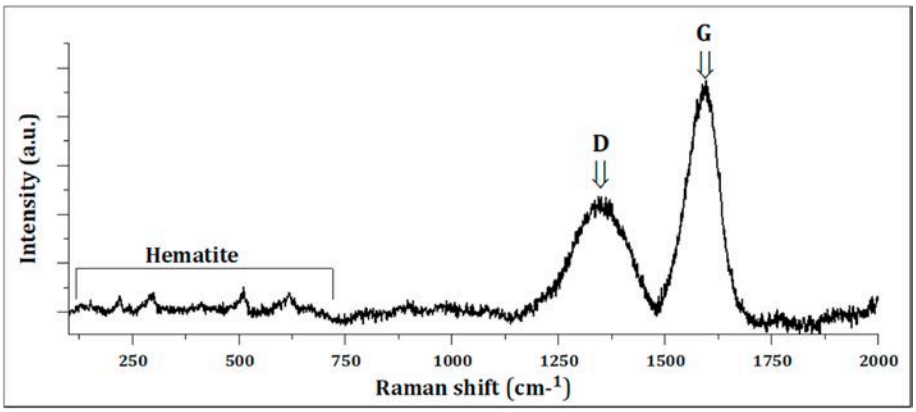

Fig. 25. Additional Raman spectrum collected at the sliding surface between the line textured surface and steel tribopairs revealing the existence of graphitic layer.

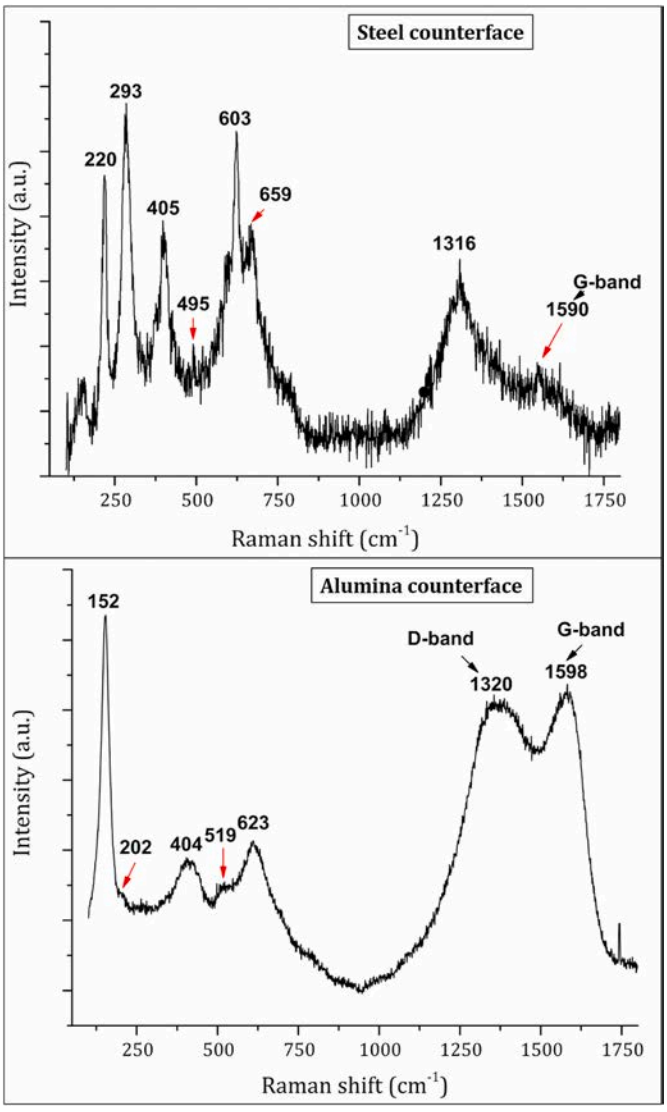

Fig. 26. Evolution of surface chemistry following dry-sliding contact between the untextured MAX phase material against the steel and alumina counterfaces.

Acknowledgement

We wish to acknowledge the Henry Royce Institute for Advanced Materials, funded through EPSRC grants EP/R00661X/1, EP/P02470X/1 and EP/P025285/1. Idris Tugrul Gulenc acknowledges the support of the Turkish Government for a PhD Studentship.

References

[1] Y. Zhang, G.P. Ding, Y. Zhou, B.C. Cai, Ti_3SiC_2-a self-lubricating ceramic, Mater. Lett. 55 (2002) 285–289.
[2] M.W. Barsoum, The $M_{N+1}AX_N$ phases: a new class of solids: thermodynamically stable nanolaminates, Prog. Solid State Chem. 28 (1) (2000) 201–281.
[3] Y. Zhou, Z. Sun, Crystallographic relations between Ti_3SiC_2 and TiC, Mater. Res. Innovat. 3 (5) (2000) 286–291.
[4] M.W. Barsoum, T. El-Raghy, Synthesis and characterization of a remarkable ceramic: Ti_3SiC_2, J. Am. Ceram. Soc. 79 (7) (1996) 1953–1956.
[5] M.W. Barsoum, The $M_{N+1}AX_N$ phases: a new class of solids, Prog. Solid State Chem. 28 (1) (2000) 201–281.
[6] M. Barsoum, M. Radovic, Mechanical properties of the MAX phases, Annu. Rev. Mater. Res. 41 (2011) 195–227.
[7] M.W. Barsoum, M. Radovic, Elastic and mechanical properties of the MAX phases, Annu. Rev. Mater. Res. 41 (1) (2011) 195–227.
[8] J. Gonzalez-Julian, Processing of MAX phases: from synthesis to applications, J. Am. Ceram. Soc. 104 (2) (2021) 659–690.
[9] P. Eklund, J.P. Palmquist, J. Höwing, D.H. Trinh, T. El-Raghy, H. Högberg, L. Hultman, Ta4AlC3: phase determination, polymorphism and deformation, Acta Mater. 55 (14) (2007) 4723–4729.
[10] M.W. Barsoum, T. El-Raghy, The MAX Phases: unique New Carbide and Nitride Materials: ternary ceramics turn out to be surprisingly soft and machinable, yet also heat-tolerant, strong and lightweight, Am. Sci. 89 (4) (2001) 334–343.
[11] J. Gruber, A.C. Lang, J. Griggs, M.L. Taheri, G.J. Tucker, M.W. Barsoum, Evidence for bulk ripplocations in layered solids, Sci. Rep. 6 (1) (2016) 33451.
[12] M. Barsoum, G. Tucker, Deformation of Layered Solids: Ripplocations Not Basal Dislocations, Scripta Materialia, 2017, p. 139.
[13] A. Murugaiah, M. Barsoum, S. Kalidindi, T. Zhen, Spherical nanoindentations and kink bands in Ti_3SiC_2, J. Mater. Res. 19 (2004).
[14] Z. Sun, Z. Zhang, H. Hashimoto, T. Abe, Ternary compound Ti_3SiC_2: Part II. Deformation and fracture behavior at different temperatures, Mater. Trans. 43 (3) (2002) 432–435.
[15] Z.-F. Zhang, Z.-M. Sun, H. Zhang, H. Hashimoto, Micron-scale deformation and damage mechanisms of Ti_3SiC_2 crystals induced by indentation, Adv. Eng. Mater. 6 (12) (2004) 980–983.
[16] S.B. Li, H.X. Zhai, A soft ceramic Ti_3SiC_2 with microscale plasticity at room temperature, Key Eng. Mater. 280–283 (2004) 1343–1346.
[17] M. Barsoum, Microscale Plasticity and Fracture Toughness of Ti_3SiC_2 at Ambient and High Temperatures, 1999, p. 32.
[18] M. Radovic, M. Barsoum, MAX phases: bridging the gap between metals and ceramics, Am. Ceram. Soc. Bull. 92 (2013) 20–27.
[19] C. Hu, Y. Sakka, S. Grasso, T. Nishimura, S. Guo, H. Tanaka, Shell-Like nano-layered Nb_4AlC_3 ceramic with high strength and toughness, Scripta Mater. 64 (2011) 765–768.
[20] S. Gupta, M.W. Barsoum, On the tribology of the MAX phases and their composites during dry sliding: a review, Wear 271 (9–10) (2011) 1878–1894.
[21] C. Alison, H.K. Erich, J.W.B. Summers, M. Sverre, Ultra-low friction for a layered carbide-derived ceramic, Ti_3SiC_2, investigated by lateral force microscopy (LFM), J. Phys. Appl. Phys. 32 (6) (1999) 632.

[22] J. Yang, W. Gu, L.M. Pan, K. Song, X. Chen, T. Qiu, Friction and wear properties of in situ (TiB_2+TiC)/Ti_3SiC_2 composites, Wear 271 (11) (2011) 2940–2946.
[23] A. Souchet, J. Fontaine, M. Belin, T. Le Mogne, J.-L. Loubet, M.W. Barsoum, Tribological duality of Ti_3SiC_2, Tribol. Lett. 18 (3) (2005) 341–352.
[24] R. Zhang, K. Feng, J. Meng, F. Liu, S. Ren, W. Hai, A. Zhang, Tribological behavior of Ti_3SiC_2 and Ti_3SiC_2/Pb composites sliding against Ni-based alloys at elevated temperatures, Ceram. Int. 42 (6) (2016) 7107–7117.
[25] S. Myhra, J.W.B. Summers, E.H. Kisi, Ti_3SiC_2—a layered ceramic exhibiting ultra-low friction, Mater. Lett. 39 (1) (1999) 6–11.
[26] T. El-Raghy, P. Blau, M.W. Barsoum, Effect of grain size on friction and wear behavior of Ti_3SiC_2, Wear 238 (2) (2000) 125–130.
[27] Y. Zhou, Z. Sun, Micro-scale plastic deformation of polycrystalline Ti_3SiC_2 under room-temperature compression, J. Eur. Ceram. Soc. 21 (8) (2001) 1007–1011.
[28] C. Magnus, W.M. Rainforth, Spark plasma sintering (SPS) synthesis and tribological behaviour of MAX phase composite of the family $Ti_{n+1}SiC_n$ (n = 2), Wear 438–439 (2019) 203062.
[29] S. Ren, J. Meng, J. Lu, S. Yang, Tribological behavior of Ti_3SiC_2 sliding against Ni-based alloys at elevated temperatures, Tribol. Lett. 31 (2008) 129–137.
[30] B.Y. Islak, D. Candar, Synthesis and properties of TiB_2/Ti_3SiC_2 composites, Ceram. Int. 47 (1) (2021) 1439–1446.
[31] H. Guo, J. Zhang, F. Li, Y. Liu, J. Yin, Y. Zhou, Surface strengthening of Ti_3SiC_2 through magnetron sputtering Cu and subsequent annealing, J. Eur. Ceram. Soc. 28 (10) (2008) 2099–2107.
[32] C. Magnus, D. Cooper, L. Ma, W.M. Rainforth, Microstructures and Intrinsic Lubricity of in Situ Ti_3SiC_2–$TiSi_2$–TiC MAX Phase Composite Fabricated by Reactive Spark Plasma Sintering (SPS), Wear, 2020, p. 203169, 448-449.
[33] W. Dang, S. Ren, J. Zhou, Y. Yu, L. Wang, The tribological properties of Ti_3SiC_2/Cu/Al/SiC composite at elevated temperatures, Tribol. Int. 104 (2016) 294–302.
[34] C. Putignano, G. Parente, F.J. Profito, C. Gaudiuso, A. Ancona, G. Carbone, Laser microtextured surfaces for friction reduction: does the pattern matter? Materials 13 (21) (2020) 4915.
[35] C.L. Zhou, T.W.L. Ngai, L.J. Li, Wetting behaviour of laser textured Ti_3SiC_2 surface with micro-grooved structures, Mater. Sci. Technol. 32 (8) (2016) 805–812.
[36] H. Costa, I. Hutchings, Some innovative surface texturing techniques for tribological purposes, Proc. IME J. J. Eng. Tribol. 229 (4) (2015) 429–448.
[37] D.G. Coblas, A. Fatu, A. Maoui, M. Hajjam, Manufacturing textured surfaces: state of art and recent developments, Proc. IME J. J. Eng. Tribol. 229 (1) (2015) 3–29.
[38] M. Martínez-Calderon, M. Manso-Silván, A. Rodríguez, M. Gómez-Aranzadi, J. P. García-Ruiz, S.M. Olaizola, R.J. Martín-Palma, Surface micro- and nano-texturing of stainless steel by femtosecond laser for the control of cell migration, Sci. Rep. 6 (1) (2016) 36296.
[39] N.P. Suh, M. Mosleh, P.S. Howard, Control of friction, Wear 175 (1) (1994) 151–158.
[40] A. Rosenkranz, H.L. Costa, M.Z. Baykara, A. Martini, Synergetic effects of surface texturing and solid lubricants to tailor friction and wear – a review, Tribol. Int. 155 (2021) 106792.
[41] I. Etsion, State of the art in laser surface texturing, J. Tribol. 127 (1) (2005) 248–253.
[42] P.G. Grützmacher, F.J. Profito, A. Rosenkranz, Multi-scale surface texturing in tribology—current knowledge and future perspectives, Lubricants 7 (11) (2019) 95.
[43] P.G. Grützmacher, A. Rosenkranz, C. Gachot, How to guide lubricants – tailored laser surface patterns on stainless steel, Appl. Surf. Sci. 370 (2016) 59–66.
[44] A. Ramesh, W. Akram, S.P. Mishra, A.H. Cannon, A.A. Polycarpou, W.P. King, Friction characteristics of microtextured surfaces under mixed and hydrodynamic lubrication, Tribol. Int. 57 (2013) 170–176.
[45] A. Kovalchenko, O. Ajayi, A. Erdemir, G. Fenske, Friction and wear behavior of laser textured surface under lubricated initial point contact, Wear 271 (9) (2011) 1719–1725.
[46] S.P. Mishra, A.A. Polycarpou, Tribological studies of unpolished laser surface textures under starved lubrication conditions for use in air-conditioning and refrigeration compressors, Tribol. Int. 44 (12) (2011) 1890–1901.
[47] S. Kac, J. Kusinski, SEM structure and properties of ASP2060 steel after laser melting, Surf. Coating. Technol. 180–181 (2004) 611–615.
[48] C. Gachot, A. Rosenkranz, L. Reinert, E. Ramos-Moore, N. Souza, M.H. Müser, F. Mücklich, Dry friction between laser-patterned surfaces: role of alignment, structural wavelength and surface chemistry, Tribol. Lett. 49 (1) (2013) 193–202.
[49] T. Ibatan, M.S. Uddin, M.A.K. Chowdhury, Recent development on surface texturing in enhancing tribological performance of bearing sliders, Surf. Coating. Technol. 272 (2015) 102–120.
[50] C. Putignano, D. Scarati, C. Gaudiuso, R. Di Mundo, A. Ancona, G. Carbone, Soft matter laser micro-texturing for friction reduction: an experimental investigation, Tribol. Int. 136 (2019) 82–86.
[51] C. Gachot, A. Rosenkranz, S.M. Hsu, H.L. Costa, A critical assessment of surface texturing for friction and wear improvement, Wear 372–373 (2017) 21–41.
[52] C. Gachot, C.-J. Hsu, S. Suarez, P. Grützmacher, A. Rosenkranz, A. Stratmann, G. Jacobs, Microstructural and chemical characterization of the tribolayer formation in highly loaded cylindrical roller thrust bearings, Lubricants 4 (2016).
[53] C.-J. Hsu, A. Stratmann, A. Rosenkranz, C. Gachot, Enhanced growth of ZDDP-based tribofilms on laser-interference patterned cylinder roller bearings, Lubricants 5 (4) (2017) 39.
[54] A. Rosenkranz, P.G. Grützmacher, C. Gachot, H.L. Costa, Surface texturing in machine elements – A critical discussion for rolling and sliding contacts, Adv. Eng. Mater. 21 (8) (2019) 1900194.
[55] M.R. Ripoll, B. Podgornik, J.e. Viintin, Finite element analysis of textured surfaces under reciprocating sliding, Wear 271 (2011) 952–959.
[56] G.S. Joshi, C. Putignano, C. Gaudiuso, T. Stark, T. Kiedrowski, A. Ancona, G. Carbone, Effects of the micro surface texturing in lubricated non-conformal point contacts, Tribol. Int. 127 (2018) 296–301.
[57] Singh, J. and M.F. Wani, Perpetual effect of laser surface texturing on tribological properties of Ti_3SiC_2/GNP composite—a fretting wear study. Int. J. Appl. Ceram. Technol..
[58] C. Magnus, J. Sharp, W.M. Rainforth, The lubricating properties of spark plasma sintered (SPS) Ti_3SiC_2 MAX phase compound and composite, Tribol. Trans. 63 (1) (2020) 38–51.
[59] C. Magnus, W.M. Rainforth, Influence of sintering environment on the spark plasma sintering of Maxthal 312 (nominally-Ti_3SiC_2) and the role of powder particle size on densification, J. Alloys Compd. 801 (2019) 208–219.
[60] S. Yuan, W. Huang, X. Wang, Orientation effects of micro-grooves on sliding surfaces, Tribol. Int. Tribol. Int. 44 (2011) 1047–1054.
[61] N. Prodanov, C. Gachot, A. Rosenkranz, F. Mücklich, M.H. Müser, Contact mechanics of laser-textured surfaces, Tribol. Lett. 50 (1) (2013) 41–48.
[62] B. He, W. Chen, Q. Jane Wang, Surface texture effect on friction of a micro-textured poly(dimethylsiloxane) (PDMS), Tribol. Lett. 31 (3) (2008) 187.
[63] C. Yu, H. Yu, G. Liu, W. Chen, B. He, Q.J. Wang, Understanding topographic dependence of friction with micro- and nano-grooved surfaces, Tribol. Lett. 53 (1) (2014) 145–156.
[64] N. Hu, J. Han, B. Hu, Orientation effects on tribological behavior of laser textured surface, J. Comput. Theor. Nanosci. 9 (12) (2012) 2113–2115, 9: pp. 2113–2115.
[65] C. DellaCorte, A.R. Zaldana, K.C. Radil, A systems approach to the solid lubrication of foil air bearings for oil-free turbomachinery 126 (2002).
[66] C. Magnus, D. Cooper, J. Sharp, W.M. Rainforth, Microstructural Evolution and Wear Mechanism of Ti_3AlC_2 – Ti_2AlC Dual MAX Phase Composite Consolidated by Spark Plasma Sintering (SPS), Wear, 2019, p. 203013, 438-439.
[67] C. Magnus, J. Sharp, W.M. Rainforth, The Lubricating Properties of Spark Plasma Sintered (SPS) Ti_3SiC_2 MAX Phase Compound and Composite, Tribology Transactions, 2019, pp. 1–14.
[68] S.H.R. Ali, Advanced Nanomeasuring Techniques for Surface Characterization, ISRN Optics, 2012, p. 859353, 2012.
[69] S. Wang, F. Yan, A. Chen, Tribological effects of laser surface texturing and residual stress, Ind. Lubric. Tribol. 70 (2017).
[70] K.R. Williams, S.G. Daniel, The running-in of engines: choice of cylinder bore finish, Proc. Inst. Mech. Eng.: Automob. Div. 8 (1) (1954) 131–152.
[71] A.V. Sreenath, N. Raman, Running-in wear of a compression ignition engine: factors influencing the conformance between cylinder liner and piston rings, Wear 38 (2) (1976) 271–289.
[72] T. Hu, L. Hu, Q. Ding, The effect of laser surface texturing on the tribological behavior of Ti-6Al-4V, Proc. IME J. J. Eng. Tribol. 226 (10) (2012) 854–863.
[73] A. Amanov, R. Tsuboi, H. Oe, S. Sasaki, The influence of bulges produced by laser surface texturing on the sliding friction and wear behavior, Tribol. Int. 60 (2013) 216–223.
[74] L. Rapoport, A. Moshkovich, V. Perfilyev, I. Lapsker, G. Halperin, Y. Itovich, I. Etsion, Friction and wear of MoS_2 films on laser textured steel surfaces, Surf. Coating. Technol. 202 (14) (2008) 3332–3340.
[75] D. Kümmel, M. Hamann-Schroer, H. Hetzner, J. Schneider, Tribological behavior of nanosecond-laser surface textured Ti6Al4V, Wear 422–423 (2019) 261–268.
[76] Q. Ding, L. Wang, L. Hu, T. Hu, Y. Wang, The pairing-dependent effects of laser surface texturing on micro tribological behavior of amorphous carbon film, Wear 274–275 (2012) 43–49.
[77] P.A. Hooper, Melt pool temperature and cooling rates in laser powder bed fusion, Addit. Manuf. 22 (2018) 548–559.
[78] K.C. Phillips, H.H. Gandhi, E. Mazur, S.K. Sundaram, Ultrafast laser processing of materials: a review, Adv. Opt Photon 7 (4) (2015) 684–712.
[79] B. Mao, A. Siddaiah, Y. Liao, P.L. Menezes, Laser surface texturing and related techniques for enhancing tribological performance of engineering materials: a review, J. Manuf. Process. 53 (2020) 153–173.
[80] M.W. Barsoum, T. El-Raghy, L. Farber, M. Amer, R. Christini, A. Adams, The topotactic transformation of Ti3SiC2 into a partially ordered cubic Ti ($C_{0.67}Si_{0.06}$) phase bythe diffusion ofSi into molten cryolite, J. Electrochem. Soc. 146 (10) (1999) 3919–3923.
[81] Y. Xing, J. Deng, X. Feng, S. Yu, Effect of laser surface texturing on Si_3N_4/TiC ceramic sliding against steel under dry friction, Mater. Des. 52 (2013) 234–245, 1980-2015.
[82] M. Bayat, A. Thanki, S. Mohanty, A. Witvrouw, S. Yang, J. Thorborg, N.S. Tiedje, J.H. Hattel, Keyhole-induced porosities in laser-based powder bed fusion (L-PBF) of Ti6Al4V: high-fidelity modelling and experimental validation, Addit. Manuf. 30 (2019) 100835.
[83] W.E. King, H.D. Barth, V.M. Castillo, G.F. Gallegos, J.W. Gibbs, D.E. Hahn, C. Kamath, A.M. Rubenchik, Observation of keyhole-mode laser melting in laser powder-bed fusion additive manufacturing, J. Mater. Process. Technol. 214 (12) (2014) 2915–2925.
[84] W. Hu, Z. Huang, Y. Wang, X. Li, H. Zhai, Y. Zhou, L. Chen, Layered ternary MAX phases and their MX particulate derivative reinforced metal matrix composite:A review, J. Alloys Compd. 856 (2021) 157313.
[85] W.K. Pang, I.M. Low, B.H. O'Connor, A.J. Studer, V.K. Peterson, Z.M. Sun, J. P. Palmquist, Comparison of thermal stability in MAX 211 and 312 phases, J. Phys. Conf. 251 (2010) 12025.
[86] W.K. Pang, I. Low, B. O'Connor, A. Studer, V. Peterson, J.-P. Palmquist, Effect of vacuum annealing on the thermal stability of Ti_3SiC_2/TiC/$TiSi_2$ composites, J. Aust. Ceram. Soc. 45 (2009) 72–77.
[87] Y. Zhou, Z. Sun, Crystallographic relations between Ti_3SiC_2 and TiC, Mater. Res. Innovat. 3 (2000) 286–291.

[88] C. Kenel, D. Grolimund, X. Li, E. Panepucci, V.A. Samson, D.F. Sanchez, F. Marone, C. Leinenbach, In situ investigation of phase transformations in Ti-6Al-4V under additive manufacturing conditions combining laser melting and high-speed micro-X-ray diffraction, Sci. Rep. 7 (1) (2017) 16358.
[89] M. El-Khoury, B. Voisiat, T. Kunze, A. Lasagni, Improving Throughput and Microstructure Uniformity in Direct Laser Interference Patterning Utilizing Top-Hat Shaped Beams, 2021.
[90] T. Zhang, H. Li, S. Liu, S. Shen, H. Xie, W. Shi, G. Zhang, B. Shen, L. Chen, B. Xiao, M. Wei, Evolution of molten pool during selective laser melting of Ti–6Al–4V, J. Phys. Appl. Phys. 52 (5) (2018) 55302.
[91] S.-B. Li, H.-X. Zhai, Synthesis and reaction mechanism of Ti_3SiC_2 by mechanical alloying of elemental Ti, Si, and C powders, J. Am. Ceram. Soc. 88 (8) (2005) 2092–2098.
[92] T. El-Raghy, M.W. Barsoum, Processing and mechanical properties of Ti_3SiC_2: I, reaction path and microstructure evolution, J. Am. Ceram. Soc. 82 (10) (1999) 2849–2854.
[93] S.J. Bennison, M.P. Harmer, Grain-growth kinetics for alumina in the absence of a liquid phase, J. Am. Ceram. Soc. 68 (1) (1985). C-22-C-24.
[94] C. Magnus, T. Galvin, L. Ma, A. Mostaed, W.M. Rainforth, Synthesis and microstructural evolution in ternary metalloceramic Ti_3SiC_2 consolidated via the Maxthal 312 powder route, Ceram. Int. 46 (10) (2020) 15342–15356. Part A.
[95] I. Yakimets, C. Richard, G. Béranger, P. Peyre, Laser peening processing effect on mechanical and tribological properties of rolling steel 100Cr6, Wear 256 (3) (2004) 311–320.
[96] A. Garcia-Giron, J.M. Romano, Y. Liang, B. Dashtbozorg, H. Dong, P. Penchev, S. S. Dimov, Combined surface hardening and laser patterning approach for functionalising stainless steel surfaces, Appl. Surf. Sci. 439 (2018) 516–524.
[97] M.V. Zhidkov, T.N. Vershinina, O.A. Golosova, S.I. Kudryashov, A.A. Ionin, Surface texturing of steel by femtosecond laser and accompanying structure/phase transformations, Opt Laser. Technol. 131 (2020) 106370.
[98] J. Han, F. Zhang, B. Van Meerbeek, J. Vleugels, A. Braem, S. Castagne, Laser surface texturing of zirconia-based ceramics for dental applications: a review, Mater. Sci. Eng. C 123 (2021) 112034.
[99] I. Low, Z. Oo, K. Prince, Effect of vacuum annealing on the phase stability of Ti_3SiC_2, J. Am. Ceram. Soc. 90 (2007) 2610–2614.
[100] Z. Zhang, Z.M. Sun, H. Hashimoto, T. Abe, Effects of sintering temperature and Si content on the purity of Ti_3SiC_2 synthesized from Ti/Si/TiC powders, J. Alloys Compd. 352 (2003) 283–289.
[101] R. Kumari, T. Scharnweber, W. Pfleging, H. Besser, J.D. Majumdar, Laser surface textured titanium alloy (Ti–6Al–4V) – Part II – studies on bio-compatibility, Appl. Surf. Sci. 357 (2015) 750–758.
[102] L. Reinert, F. Lasserre, C. Gachot, P. Grützmacher, T. MacLucas, N. Souza, F. Mücklich, S. Suarez, Long-lasting solid lubrication by CNT-coated patterned surfaces, Sci. Rep. 7 (1) (2017) 42873.
[103] Y. Xing, X. Wang, Z. Du, Z. Zhu, Z. Wu, L. Liu, Synergistic effect of surface textures and DLC coatings for enhancing friction and wear performances of Si_3N_4/TiC ceramic, Ceram. Int. (2021).
[104] Z. Wu, J. Deng, Y. Xing, H. Cheng, J. Zhao, Effect of surface texturing on friction properties of WC/Co cemented carbide, Mater. Des. 41 (2012) 142–149.
[105] D. He, S. Zheng, J. Pu, G. Zhang, L. Hu, Improving tribological properties of titanium alloys by combining laser surface texturing and diamond-like carbon film, Tribol. Int. 82 (2015) 20–27.
[106] S.T.r. Oktay, N.P. Suh, Wear debris formation and agglomeration, J. Tribol. 114 (2) (1992) 379–393.
[107] W. Zhang, S. Yamashita, H. Kita, Effect of counterbody on tribological properties of B_4C–SiC composite ceramics, Wear 458–459 (2020) 203418.
[108] S. Gupta, D. Filimonov, T. Palanisamy, M. Barsoum, Tribological behavior of select MAX phases against Al_2O_3 at elevated temperatures, Wear 265 (2008) 560–565.
[109] J.D. Lemm, A.R. Warmuth, S.R. Pearson, P.H. Shipway, The influence of surface hardness on the fretting wear of steel pairs—its role in debris retention in the contact, Tribol. Int. 81 (2015) 258–266.
[110] A. Arslan, H.H. Masjuki, M. Varman, M.A. Kalam, M.M. Quazi, K.A.H. Al Mahmud, M. Gulzar, M. Habibullah, Effects of texture diameter and depth on the tribological performance of DLC coating under lubricated sliding condition, Appl. Surf. Sci. 356 (2015) 1135–1149.
[111] S. Thrush, A. Comfort, J. Dusenbury, X. Han, G. Barber, X. Wang, H. Qu, Wear mechanisms of a sintered tribofilm in boundary lubrication regime, Wear 482–483 (2021) 203932.
[112] H. Kato, K. Komai, Tribofilm formation and mild wear by tribo-sintering of nanometer-sized oxide particles on rubbing steel surfaces, Wear 262 (2007) 36–41.
[113] V.n.v. Munagala, S. Bessette, R. Gauvin, R. Chromik, Sliding wear of cold sprayed Ti6Al4V coatings: effect of porosity and normal load, Wear 450–451 (2020) 203268.
[114] A. Mirzaei, K. Janghorban, B. Hashemi, S. Hosseini, M. Bonyani, S. Leonardi, A. Bonavita, G. Neri, Synthesis and characterization of mesoporous α-Fe_2O_3 nanoparticles and investigation of electrical properties of fabricated thick films, Process. Appl. Ceram. 10 (2016) 209–217.
[115] A. Jubb, H. Allen, Vibrational spectroscopic characterization of hematite, maghemite, and magnetite thin films produced by vapor deposition, ACS Appl. Mater. Interfaces 2 (2010).
[116] A.C. Fernandes, L. Cunha, C. Moura, F. Vaz, P. Carvalho, E. Le Bourhis, P. Goudeau, J.P. Rivière, N.M.G. Parreira, The effect of bombarding conditions on the properties of multifunctional Ti–C–O thin films grown by magnetron sputtering, Surf. Coating. Technol. 202 (4) (2007) 946–951.
[117] C. Hunter, M. Check, C. Hager Jr., A. Voevodin, Tribological properties of carbon nanopearls synthesized by nickel-catalyzed chemical vapor deposition, Tribol. Lett. 30 (2008) 169–176.
[118] Z. Lv, J. Dang, H. Sun, Synthesis of titanium oxycarbide in TiO_2-C-H_2 system, Mater. Chem. Phys. 252 (2020) 123272.
[119] E.J. Ekoi, A. Gowen, R. Dorrepaal, D.P. Dowling, Characterisation of titanium oxide layers using Raman spectroscopy and optical profilometry: influence of oxide properties, Results. Phys. 12 (2019) 1574–1585.
[120] S.K. Sharma, B.V.M. Kumar, Y.-W. Kim, Effect of WC addition on sliding wear behavior of SiC ceramics, Ceram. Int. 41 (3) (2015) 3427–3437. Part A.
[121] S. Guicciardi, D. Sciti, C. Melandri, G. Pezzotti, Dry sliding wear behavior of nano-sized SiC pins against SiC and Si_3N_4 discs, Wear 262 (5) (2007) 529–535.
[122] P. Lu, R.J.K. Wood, M.G. Gee, L. Wang, W. Pfleging, A novel surface texture shape for directional friction control, Tribol. Lett. 66 (1) (2018) 51.
[123] Y. Wan, D.-S. Xiong, The effect of laser surface texturing on frictional performance of face seal, J. Mater. Process. Technol. 197 (1) (2008) 96–100.
[124] T.-C. Wu, S.S. Joshi, Y.-H. Ho, M.V. Pantawane, S. Sinha, N.B. Dahotre, Microstructure and surface texture driven improvement in in-vitro response of laser surface processed AZ31B magnesium alloy, J. Magnes. Alloys 9 (4) (2021) 1406–1418.
[125] M.S. Uddin, T. Ibatan, S. Shankar, Influence of surface texture shape, geometry and orientation on hydrodynamic lubrication performance of plane-to-plane slider surfaces, Lubric. Sci. 29 (3) (2017) 153–181.
[126] Y.L. Zhang, X.G. Zhang, G. Matsoukas, Numerical study of surface texturing for improving tribological properties of ultra-high molecular weight polyethylene, Biosurface and Biotribology 1 (4) (2015) 270–277.
[127] R. Rahmani, A. Shirvani, H. Shirvani, Optimization of partially textured parallel thrust bearings with square-shaped micro-dimples, Tribol. Trans. 50 (3) (2007) 401–406.
[128] P. Lu, R.J.K. Wood, M.G. Gee, L. Wang, W. Pfleging, The friction reducing effect of square-shaped surface textures under lubricated line-contacts—an experimental study, Lubricants 4 (3) (2016) 26.
[129] C. Magnus, J. Sharp, L. Ma, W.M. Rainforth, Ramification of thermal expansion mismatch and phase transformation in TiC-particulate/SiC-matrix ceramic composite, Ceram. Int. 46 (12) (2020) 20488–20495.
[130] C. Dayson, Surface temperatures at unlubricated sliding contacts, A S L E Trans. 10 (2) (1967) 169–174.
[131] F.H. Stott, High-temperature sliding wear of metals, Tribol. Int. 35 (8) (2002) 489–495.
[132] F.H. Stott, M.P. Jordan, The effects of load and substrate hardness on the development and maintenance of wear-protective layers during sliding at elevated temperatures, Wear 250 (2001) 391–400.

Carl Magnus[a,*], Idris T. Gulenc[b], W.M. Rainforth[a]
[a] *The Henry Royce Institute and Department of Engineering Materials, The University of Sheffield, Sir Robert Hadfield Building, Sheffield, S1 3JD, UK*
[b] *The Department of Materials Science & Engineering, The University of Sheffield, Sir Robert Hadfield Building, Sheffield, S1 3JD, UK*

[*] Corresponding author.
E-mail address: c.magnus@sheffield.ac.uk (C. Magnus).